Doctoral Dissertation

First-Principles Study on Electronic Structures and Electron-Transport Properties of Low-Dimensional Systems: Graphene, Carbon Nanotube, Gold Nanowire, and Porphyrin Wire

Huy Duy Nguyen

July 2014

Graduate School of Engineering
Osaka University

OSAKA UNIVERSITY

Abstract

Department of Precision Science and Technology
Graduate School of Engineering

Doctor of Philosophy in Engineering

First-Principles Study on Electronic Structures and Electron-Transport Properties of Low-Dimensional Systems: Graphene, Carbon Nanotube, Gold Nanowire, and Porphyrin Wire

by Huy Duy NGUYEN

The field of nanoscience is considered one of the key research issues of this century. The challenge is to achieve a detailed understanding of the interaction of nanostructures, both among themselves and with their macroscopic environment, and to precisely control and manipulate their properties in order to pave the way for new functionalities. The needs for further integration of electronic circuits and for continuous miniaturization in communication technology, chemical analytics, data recording, and electromechanical sensing create the driving force for current research activities. Making use of a nanodevice in a real-world application implies the interaction of the nanostructure with the macroscopic world controlling its properties by an external access. Consequently, the goal of the research in nanoscience is at first to obtain a deep understanding of the interaction of nanostructures with each other and with the macroscopic world. This understanding is a prerequisite of the second goal to gain control over their properties in order to use their intrinsic functionalities in devices or other future applications. The most promising properties for potential applications include magnetic properties (for recording and signaling), electronic transport behavior (for integrated circuits), mechanical properties (for sensing) and new emerging functionalities based on the combination of the aforementioned properties. All of these properties are governed by the electronic system of the nanostructure which itself is strongly coupled to structural quantities. Since all these quantities are tightly linked, it is mandatory to study them in a comprehensive and fundamental way on a well-chosen selection of model systems. In this thesis, by using first-principles calculations within the framework of density functional theory, I study the electronic structures and electron-transport properties of low-dimensional systems comprising of: (1) graphene with absorbed transition-metal adatoms, (2) carbon/boron-nitride nanotubes, (3) carbon-incorporated gold nanowires, and (4) thiol-terminated zinc porphyrin wires. The thesis is organized as follows.

Chapter 1 gives a general introduction about low-dimensional systems and their interest in nanoscience and nanotechnology.

Chapter 2 describes the computational methods which are employed in this thesis. The basic ideas behind density functional theory, pseudopotentials, and real-space finite-difference formalism are briefly reviewed and presented. This chapter also includes techniques for studying the electron-transport property, the treatment of spin-orbit coupling and magnetic anisotropy energy.

Chapter 3 is dedicated to the electronic structures and magnetic properties of graphene with an absorbed Fe, Co, or Ni adatom. Recent scanning tunneling microscopy experiment reported the deposition of single Fe, Co, or Ni adatom on graphene, which can tune the electronic structures and realize the spin texture of the graphene at the same time. The experimental observation found that both the Fe and Co adatoms prefer an

out-of-plane easy magnetization axis. On the other hand, previous density functional theory studies suggested that the Co adatom exhibits an out-of-plane easy axis, whereas the Fe adatom shows an in-plane easy axis. The number of theoretical studies is limited and do not provide sufficient results to discuss the discrepancy with the experiment in detail. By inclusion of spin-orbit coupling, electronic structures and magnetic anisotropy energies of graphene with adsorbed Fe, Co, or Ni adatom are investigated. The results show that spin polarizations are observed in the case of the Fe and Co adsorption. In the case of Ni adsorption, the Rashba effect is realized with a **k**-dependent energy shift at the bottom of the Fermi surface of π bands. The calculated magnetic anisotropy energies indicate that the Fe adatom exhibits an in-plane easy axis, in contradiction with experiment, whereas the Co adatom favors an out-of-plane easy axis, in agreement with experimental observation. It is found that the occupation of E_1 orbitals, which comprises of d_{xz} and d_{yz} orbitals, is important to explain the magnetic anisotropy in the Fe and Co adatoms. This results are expected to stimulate the interest in the usage of graphene as magnetized medium in magnetic storage.

Chapter 4 discusses the electronic structures and electron-transport properties of carbon/boron-nitride nanotubes. At the zigzag carbon edges of graphene nanostructures and carbon nanotubes, localized edge states are usually observed which act as a source of magnetism and spin-dependent transport. By laser vaporization method, carbon/boron-nitride nanotube in which carbon and boron-nitride nanotubes are alternately placed along the tube axis was fabricated. This structure is of interest because from first-principles calculations, it was found that magnetic ordering could be realized by carrier doping. In addition, the magnetic ground states are associated with edge states at the zigzag edges of carbon nanotube. However, carrier doping is not practical when this material is connected to electrodes. Furthermore, the rotational symmetry mismatch between the conducting and edge states of a zigzag carbon nanotube prevents electron transport. Therefore, the spin-dependent transport through the carbon/boron-nitride nanotubes has not been investigated so far. By first-principles calculations, the electronic structures and electron-transport properties of carbon/boron-nitride nanotube are studied. It was found that edge states emerge at zigzag boundary between carbon and boron-nitride nanotubes. The variation of the occupation number of the edge states gives rise to the spin polarization by p-type substitutional doping at the zigzag carbon nanotube edge. The σ-π hybridization due to the curvature pulls down the energetically dispersive states, resulting in the nonmagnetic ground-state electronic structure in the case of n-type doping. Although it has been reported that the electron transport through the edge states in the undoped nanotube is suppressed by the rotational symmetry mismatch between the edge and carbon nanotube states, the calculations point out that the alternation of the symmetry due to doped atom leads to the spin-dependent

resonant tunneling through the edge states. The results suggest the use of this nanotube as channel material in a spin field-effect transistor.

Chapter 5 investigates the electronic structures of gold nanowires with carbon incorporation. Gold nanowires have been fabricated by scanning tunneling microscopy and break junction techniques. By these methods, the gold nanowire has the interatomic distances typically around 3.0 Å and 3.6 Å. Recent experiment using transmission electron microscopy combined with scanning tunneling microscopy pointed out that it was possible to fabricate gold nanowires with long interatomic distance of 5.0 Å. The long atomic spacing was attributed to the incorporation of carbon atoms with evidence of fullerene as the tip. Furthermore, the gold surface seemed to be reconstructed by adsorbed carbon atoms to form one-dimensional nanowires. Although theoretical investigations on these structures are necessary, no studies have been carried out so far. By first-principles calculations, the electronic structures of gold nanowires with zero, one, two, and three carbon atoms insertion, both in vacuum and on gold (111) surface are investigated. The results show that, in vacuum, two carbon atoms are found to link neighboring gold atoms resulting in the largest breaking force of the nanowire and an anomalously long gold interatomic distance of 5.0 Å. The calculation results are in excellent agreement with the experiment. On gold (111) surface, the gold nanowire with two carbon atoms insertion possess the gold interatomic distance of 5.0 Å, close to the value observed experimentally. In addition, the calculated formation energies indicate that the gold nanowire with two carbon atoms insertion is the most stable structure. The results suggest that gold nanowires may be formed on the surface before pulling of the gold tips. These findings are important for understanding the formation and fabrication of gold nanowires.

Chapter 6 focuses on the electronic structures and electron-transport properties of thiol-terminated zinc porphyrin wires connected to gold electrodes. Single molecule switch utilizing zinc porphyrin molecules has been fabricated using scanning tunneling microscopy tips. The measured conductance spectra showed the traces of low- and high-conductance upon pulling the tips. The origin of the observed dual conductance may be related to the differences in contact geometry between porphyrin molecule and gold electrodes using thiol linker. However, no first-principles studies have been carried out on these systems. By first-principles calculations, the electron-transport properties of thiol-linked porphyrin molecule suspended between gold (111) electrodes are investigated. Two structures, in which sulphur atoms of the porphyrin molecule are situated on the hollow site of gold electrode and are linked to gold adatoms on gold electrode, are considered. The results show that the highest occupied molecular orbitals of two structures have different characteristics, indicating two different transport modes, in agreement with the experiment. The studied results are expected to give interest in using porphyrin molecules as components in molecular switches.

Contents

List of Figures

List of Tables

Chapter 1

Introduction

Nanoscience and nanotechnology are the study of phenomena and manipulation of materials at atomic, molecular, or macromolecular scales. When one or more spatial dimensions of a material are small, typically 100 nanometers or less, enough to restrict the quantum mechanical wavefunction of electrons contained inside, a low-dimensional system is realized. This is achieved by trapping electrons in a narrow potential well that confines their motions to discrete energy levels. If the separation between these energy levels is large enough, the electrons will appear to be frozen into the ground state and no motion will be possible in this dimension. This results in a two-dimensional electron gas. The same process can be achieved with a two-dimensional potential well, resulting in a quantum wire.

At the quantum-realm scale, properties of a material, such as energy, change owing to the manifestation of quantum effects which are very different from those when the same material is in a bulk form. The same metal can become a semiconductor or an insulator when the nanoscale level is reached. In particular, quantization of conductance can be observed for a quantum wire. In such a wire, the conductance (for a single conductance channel) is quantized in units of:

$$G = \frac{2e^2}{h}T.$$

This equation is known as Landauer–Büttiker formula. If the transmission probability $T = 1$, i.e., no elastic scattering inside the quantum wire, G reduces to the well-known conductance quantum $G_0 = (12.9\text{k}\Omega)^{-1}$.

Another exceptional property of low-dimensional systems is that they can be fabricated atom-by-atom with a bottom-up process. The information for this fabrication is embedded in the material building blocks so that they can self-assemble in the final product.

Low-dimensional systems also have an increased surface to volume ratio compared to bulk systems, which have important consequences on processes such as catalysis or detection at a material surface.

Thus, for the needs of further integration and miniaturization of electronic circuits and devices, a deep understanding of the properties of low-dimensional systems such as magnetic properties, electron transport behavior, mechanical properties, has become of utmost importance. In this thesis, I use first-principles calculations based on density functional theory to study the electronic structures and electron-transport properties of low-dimensional systems, which consist of: (1) graphene with adsorbed transition-metal adatoms for applications in magnetic storage, (2) carbon/boron-nitride nanotubes for applications in spin field-effect transistor, (3) carbon-incorporated gold nanowires for the understanding of the fabrication of gold nanowires, and (4) thiol-linked zinc porphyrin wires for applications in molecular switch.

The thesis is presented as followings. In chapter 2, theoretical background employed in the calculations is discussed. Chapter 3 focuses on the magnetic properties of graphene with an absorbed Fe, Co, or Ni adatom. Chapter 4 deals with electronic structures and electron-transport property of carbon/boron-nitride nanotubes. Chapter 5 studies the electronic structures of carbon-incorporated gold nanowires. Chapter 6 investigates the electronic structures and electron-transport properties of thiol-linked zinc porphyrin wires. Finally, the major findings and concluding remarks are given.

Chapter 2

Computational Procedures

First-principles calculations were done using a first-principles simulation code named "RSPACE" developed by Prof. Tomoya Ono of Department of Precision Science and Technology, Graduate School of Engineering, Osaka University. In this chapter, the computational procedures and techniques employed in my studies are presented.

2.1 Density functional theory

2.1.1 Kohn-Sham equation

In solid-state physics, the ground-state energy of a system consisting of N interacting particles is obtained by solving the corresponding Schrödinger equation (as Born-Oppenheimer approximation is applied):

$$H\psi = E\psi, \tag{2.1}$$

$$(T + V_{ion-ele} + V_{ele-ele})\psi = E\psi, \tag{2.2}$$

where

T is the kinetic energy operator,

$V_{ion-ele}$ is the electron-nucleus attraction energy operator,

$V_{ele-ele}$ is the electron-electron repulsion energy operator,

$\psi = \psi(1, 2, \ldots N)$ is the wave function of the N-particle system,

and E is the energy of the N-particle system.

The ground-state energy is then obtained by minimizing the energy of the N-particle system with respect to the wave function ψ, according to variational principle:

$$\delta(\langle\psi|H|\psi\rangle - E\langle\psi|\psi\rangle) = 0. \tag{2.3}$$

In the classical limit, it is not easy to solve this equation because the wave function ψ has many degrees of freedom. Thus, minimizing the energy with respect to ψ as a variable is inefficient. In addition, T and $V_{ele-ele}$ in equation (2.2) only represent the kinetic energy and Coulomb interaction of a free electron gas, and include no contribution from the quantum effects of an interacting system. This gives rise to the error in the results of (2.2), which was illustrated in Hartree-Fock scheme. The density functional theory (DFT), on the other hand, states that the energy E can be considered as a functional of charge density ρ, as proven by Hohenberg-Kohn theorems [7]. Then, the ground-state energy is found by minimizing the energy E with respect to ρ, according to variational principle:

$$\delta(E[\rho] - \mu(\int \rho(\mathbf{r})d\mathbf{r} - N) = 0, \tag{2.4}$$

where μ is Lagrange multiplier and N is the number of particles. The other operators in (2.2) can also be expressed as functionals of charge density, and the Schrödinger equation is rewritten in the form of Kohn-Sham equations [8]:

$$(-\frac{1}{2}\nabla^2 + v_{ion}[\rho] + v_H[\rho] + v_{XC}[\rho])\psi_i = \epsilon_i\psi_i, \tag{2.5}$$

and

$$\rho(\mathbf{r}) = \sum_i^N \sum_s |\psi_i(\mathbf{r}, s)|^2, \tag{2.6}$$

where,

v_{ion} is the *ionic potential* due to electron-ion interaction,

v_H is the *Hartree potential* due to electron-electron interaction,

v_{XC} is the *exchange-correlation potential* coming from the quantum effects of interacting electrons,

and ψ_i is the one-electron wave function of non-interacting particles, called Kohn-Sham orbital.

The reason why we can change from wave function ψ of an interacting system to the wave functions ψ_i of a non-interacting system is complicated and will not be proven here. Because the potentials in (2.5) are dependent on the charge density ρ, the ground-state

energy is thus found by iterative method. First, an initial charge density is given to (2.5) in order to get the solution of Kohn-Sham orbitals ψ_i. Then, a new charge density is obtained by (2.6), and will, in turn, be put back to (2.5). Therefore, (2.5) and (2.6) create a loop where the energy is minimized until a specific criterion for convergence is reached.

The exchange-correlation (XC) potential within DFT in (2.5) is the universal functional of charge density, meaning that the same functional for any systems from molecules to crystals. However, the exact formula for the XC potential is unknown. There have been several approximations to the XC potential, which are known to give reasonable results. One of these is the Local Spin Density Approximation (LSDA), which is discussed in the next section.

2.1.2 Local spin density approximation

As already discussed by Kohn and Sham, solids can often be considered as close to the limit of the homogeneous electron gas. In that limit, it is known that the effects of exchange and correlation are local in character, and they proposed making the local density approximation (LDA) (or more generally the LSDA), in which the exchange-correlation energy is simply an integral over all space with the exchange-correlation energy density at each point assumed to be the same as in a homogeneous electron gas with that density,

$$\begin{aligned} E_{XC}^{LSDA}[\rho^{\uparrow},\rho^{\downarrow}] &= \int d\mathbf{r}\,\rho(\mathbf{r})\epsilon_{XC}^{hom}(\rho^{\uparrow},\rho^{\downarrow}) \\ &= \int d\mathbf{r}\,\rho(\mathbf{r})\Big[\epsilon_{X}^{hom}(\rho^{\uparrow},\rho^{\downarrow}) + \epsilon_{C}^{hom}(\rho^{\uparrow},\rho^{\downarrow})\Big], \end{aligned} \tag{2.7}$$

where $\epsilon_X^{hom}(\rho^{\uparrow},\rho^{\downarrow})$ and $\epsilon_C^{hom}(\rho^{\uparrow},\rho^{\downarrow})$ indicate the exchange and correlation energies per particle of a uniform electron gas of density $(\rho^{\uparrow},\rho^{\downarrow})$. The LSDA is the most general local approximation and is given explicitly for exchange and by approximate (or fitted) expressions for correlation. For unpolarized systems, the LDA is found simply by setting $\rho^{\uparrow}(r) = \rho^{\downarrow}(r) = \rho(r)/2$. Once one has made the local ansatz for the L(S)DA, then all the rest follows. Since the functional $E_{XC}[\rho^{\uparrow},\rho^{\downarrow}]$ is universal, it follows that it is exactly the same as for the homogeneous gas. The only information needed is the exchange-correlation energy of the homogeneous gas as a function of density; the exchange energy of the homogeneous gas can be given by a simple analytic form and the correlation energy has been calculated to great accuracy with Monte Carlo method [9]. In the LDA, the

form for XC term is very simple,

$$\delta E_{XC}[\rho] = \sum_{\sigma} \int d\mathbf{r} \left[\epsilon_{XC}^{hom} + \rho \frac{\partial \epsilon_{XC}^{hom}}{\partial \rho^{\sigma}} \right]_{\mathbf{r},\sigma} \delta\rho(\mathbf{r}) \tag{2.8}$$

so that the potential,

$$V_{XC}^{\sigma} = \left[\epsilon_{XC}^{hom} + \rho \frac{\partial \epsilon_{XC}^{hom}}{\partial \rho^{\sigma}} \right]_{\mathbf{r},\sigma} \tag{2.9}$$

involves only ordinary derivatives of $\epsilon_{XC}^{hom}(\rho^{\uparrow}, \rho^{\downarrow})$. Here the subscript $\mathbf{r}, \sigma$ means the quantities in square brackets are evaluated for $\rho^{\sigma} = \rho(\mathbf{r}, \sigma)$. The LDA exchange part is particularly simple: since $\epsilon_{X}^{hom}(\rho^{\sigma})$ scales $(\rho^{\sigma})^{\frac{1}{3}}$ it follows that

$$V_{X}^{\sigma}(\mathbf{r}) = \frac{4}{3} \epsilon_{X}^{hom}(\rho(\mathbf{r}, \sigma)). \tag{2.10}$$

The underlying reason for using the local approximation is that for the densities typical of those found in solids, the range of the effects of exchange and correlation is rather short. However, this is not justified by a formal expansion in some small parameter, and one must test the extent to which it works by actual applications. It is expected that it will be best for solids close to a homogeneous gas (like a nearly-free-electron metal), and worst for very inhomogeneous cases like atoms, where the density must go continuously to zero outside the atom.

Among the most obvious faults of LDA is the spurious self-interaction term. In the Hartree-Fock approximation, the unphysical self-interaction term in the Hartree interaction is exactly cancelled by the non-local exchange interaction. However, in the local approximation to the exchange interaction, the cancellation is only approximate and there remain spurious self-interaction terms that are negligible in the homogeneous gas but large in confined systems such as atoms. Nevertheless, even in very inhomogeneous cases, the LDA is found to work remarkably well.

2.1.3 Pseudopotentials

2.1.3.1 Norm-conserving pseudopotentials

The calculations including core electrons greatly increase the computational cost since the wave functions of core electrons strongly oscillate in the vicinity of the atomic nuclei and a high cutoff energy for plane waves or a small grid spacing is required. In addition, the behavior of core electrons of molecules and crystals in practice is similar to that of electrons in an isolated atom, and valence electrons of atoms determine most of the properties of the material. Thus, the pseudopotential is introduced as an effective

potential to replace the atomic all-electron potential such that core states are eliminated and the valence electrons are described by pseudo-wave functions.

The most frequently used pseudopotential in DFT calculations is the norm-conserving pseudopotential [10–12]. The pseudo-wave function obtained using these pseudopotentials has the following desirable properties (see Fig. 2.1):

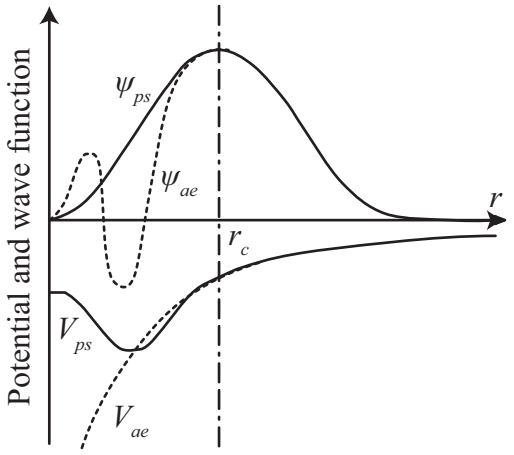

FIGURE 2.1: Illustration of pseudopotential V_{ps} and pseudo-wave function ψ_{ps}. V_{ae} is the pseudopotential obtained by the all-electron calculation and u_{ae} is the all-electron wave function. r_c is the core radius.

1. The pseudo-wave function contains no nodes.
2. The pseudo- and all-electron wave function agree beyond the core radius of r_{c}.
3. The eigenvalues of the valence electron states using pseudopotentials agree with the eigenvalues calculated including the core electrons.
4. Up to the core radius of r_c, the norm $\int_0^{r_c} |R_{ps}(r)r|^2\, dr$ of the pseudo-wave function coincides with the norm of the all-electron wave function. Here, $R_{ps}(r)$ is the radial component of the wave function $\psi(\mathbf{r}) = R_{ps}(r)Y(\theta,\phi)$, r is the distance from the nucleus, and $Y(\theta,\phi)$ is a spherical harmonic function.

2.1.3.2 Projector augmented-wave method

The norm-conserving pseudopotential method has the merit of formal simplicity. Unfortunately, this formal simplicity has a price: when applied to a system with d or f electrons, very large or complicated basis sets instead of plane waves have to be used. Similarly for early transition-metal elements and rare earth metals, treating semicore states as valence states often results in hard pseudopotentials and affects the transferability. Vanderbilt's ultrasoft pseudopotentials [13, 14] have improved this situation

significantly by relaxing the norm-conserving condition. This method also allows first-row and transition-metal elements to be treated in an efficient way.

Since wave functions of real materials have very different behavior in different regions of space (fairly smooth in the bonding region whereas rapidly oscillating close to the nucleus), the strategy of the augmented-wave methods is to divide the wave function into a partial-wave expansion within an atom-centered sphere and envelope functions outside the spheres. The envelope function is expanded into plane waves or some other convenient basis set. Envelope function and partial-wave expansions are then matched with value and derivative at the sphere radius.

Consider the Hilbert space of all wave functions orthogonal to the core states. The all-electron (AE) wave functions of this Hilbert space will be transformed into new pseudo (PS) wave functions of a PS Hilbert space by a linear transformation. An AE wave function is a full one-electron Kohn-Sham wave function and is not to be confused with a many-electron wave function. From now on, the quantities associated with the PS representation of the wave functions will be indicated by a tilde.

By the transformation from the PS wave functions to the AE wave functions, the physical quantities, which are represented by the expectation value $\langle \mathcal{A} \rangle$ of a certain operator $\mathcal{A}$, can be obtained from the PS wave functions $|\tilde{\Psi}\rangle$ either directly as $\langle \Psi | \mathcal{A} | \Psi \rangle$ after transformation to the true AE wave functions $|\Psi\rangle = \mathcal{T}|\tilde{\Psi}\rangle$ or as the expectation value $\langle \mathcal{A} \rangle = \langle \tilde{\Psi} | \tilde{\mathcal{A}} | \tilde{\Psi} \rangle$ of a PS operator $\tilde{\mathcal{A}} = \mathcal{T}^\dagger \mathcal{A} \mathcal{T}$ in the Hilbert space of the PS wave functions. The ground-state PS wave functions can be obtained from

$$\frac{\partial E[\mathcal{T}|\tilde{\Psi}]}{\partial \langle \tilde{\Psi}|} = \epsilon \mathcal{T}^\dagger \mathcal{T} |\tilde{\Psi}\rangle. \tag{2.11}$$

Let us consider only the transformations that differ from identity by a sum of local, atom-centered contributions $\tilde{\mathcal{T}}_R$ such that

$$\mathcal{T} = 1 + \sum_R \tilde{\mathcal{T}}_R. \tag{2.12}$$

Each local contribution $\tilde{\mathcal{T}}_R$ acts only within the augmentation region Ω_R around the atom. Thus, the AE and PS wave functions agree outside the augmentation regions. The augmentation region in the pseudopotential method corresponds to the so-called core region.

The local contributions $\tilde{\mathcal{T}}_R$ are defined for each augmentation region individually. This is done by specifying the target functions $|\phi_i\rangle$ of the transformation $\mathcal{T}$ for a set of initial functions $|\tilde{\phi}_i\rangle$, which is orthogonal to the core states and complete in the augmentation region, by $|\phi_i\rangle = (1 + \tilde{\mathcal{T}}_R)|\tilde{\phi}_i\rangle$ within Ω_R. The initial states $|\tilde{\phi}_i\rangle$ and the corresponding

target functions $|\phi_i\rangle$ are called PS and AE partial waves, respectively. Naturally, a choice for the AE partial waves would be the solutions of the radial Schrödinger equation for the isolated atom. Here, the index i indicates the atomic site $\mathcal{R}$, the angular momentum quantum numbers $\mathcal{L} = (l, m)$, and an index n to denote different partial waves for the same site and angular momentum. For each AE partial wave, a PS partial wave denoted by $|\tilde{\phi}_i\rangle$ is defined. The PS partial waves must coincide with the corresponding AE partial waves outside the augmentation region and form a complete set of functions within the augmentation region.

Within the augmentation region, each PS wave function can be expressed as the sum of PS partial waves:

$$|\tilde{\Psi}\rangle = \sum_i |\tilde{\phi}_i\rangle c_i \text{ within } \Omega_R. \tag{2.13}$$

Since $|\phi_i\rangle = \mathcal{T}|\tilde{\phi}\rangle$, the corresponding AE wave function has the form

$$|\Psi\rangle = \mathcal{T}|\tilde{\Psi}\rangle = \sum_i |\phi_i\rangle c_i \text{ within } \Omega_R, \tag{2.14}$$

with identical coefficients c_i in both expansions. Hence the AE wave functions can be expressed as

$$|\Psi\rangle = |\tilde{\Psi}\rangle - \sum_i |\tilde{\phi}_i\rangle c_i + \sum_i |\phi_i\rangle c_i, \tag{2.15}$$

where the expansion coefficients for the partial wave expansions need to be determined.

Since the transformation $\mathcal{T}$ is linear, the coefficients must be linear functionals of the PS wave functions and are scalar products

$$c_i = \langle \tilde{p}_i | \tilde{\Psi} \rangle \tag{2.16}$$

of the PS wave function with some fixed functions $\langle \tilde{p}_i|$, called projector functions. There is exactly one projector function for each PS partial wave. The projector functions must satisfy the condition $\sum_i |\tilde{\phi}_i\rangle\langle\tilde{p}_i| = 1$ within Ω_R, so that the one-center expansion $\sum_i |\tilde{\phi}_i\rangle\langle\tilde{p}|\tilde{\Psi}\rangle$ of a PS wave function is identical to the PS wave function $\tilde{\Psi}$ itself. This means that

$$\langle \tilde{p}_i | \tilde{\phi}_j \rangle = \delta_{ij}. \tag{2.17}$$

The projector functions are chosen to be localized in the augmentation region, although extended projector functions could also be adopted. The most general form for the projector functions is $\langle \tilde{p}_i = \sum_i (\langle f_k | \tilde{\phi}_l \rangle)^{-1}_{ij} \langle f_l|$, and the set of $|f_j\rangle$ forms an linearly independent set of functions. The projector functions are localized if the functions $|f_j\rangle$ are localized.

In summary, a linear transformation

$$\mathcal{T} = 1 + \sum_i (|\phi_i\rangle - |\tilde{\phi}_i\rangle)\langle\tilde{p}_i| \tag{2.18}$$

between the valence wave functions and PS wave functions is the spirit of the projector-augmented wave method. With this transformation, the AE wave function is obtained from the PS wave function by

$$|\Psi\rangle = |\tilde{\Psi}\rangle + \sum_i (|\phi_i\rangle - |\tilde{\phi}_i\rangle)\langle\tilde{p}_i|\tilde{\Psi}\rangle. \tag{2.19}$$

The quantities that determine this transformation are (i) the AE partial waves $|\phi_i\rangle$, which are orthogonalized to the core states and are obtained by radially integrating the Schrödinger equation of the atomic energy for a set of energies ϵ_i; (ii) one PS partial wave $|\tilde{\phi}_i\rangle$, which agrees with the corresponding AE partial wave outside some augmentation region for each AE partial wave; and (iii) one projector function $\langle\tilde{p}_i|$ for each PS partial wave localized within the augmentation region and obeys the relation $\langle\tilde{p}_i|\tilde{\phi}_j\rangle = \delta_{ij}$.

2.2 Real-space finite-difference formalism

In finite-difference method, the real space is divided into grid points, and the wave functions, charge density as well as the quantities in the Kohn-Sham equation (2.5) are evaluated at the grid points only. When solving the Kohn-Sham equation, the derivations of potentials with respect to the wave functions are frequently performed. Considering the one-dimensional case, within the finite-difference formalism, the k-th order of a function $f(x)$ at a grid point $x = ih$, where i is an integer, is approximated by the finite-difference formulas [15]

$$\frac{\mathrm{d}^{(k)}}{\mathrm{d}x^{(k)}} f(x)|_{x=ih} = \sum_{n=-N_f}^{N_f} c_n^{(k)} f(ih + nh). \tag{2.20}$$

Here, h is the grid spacing and N_f is the order of the finite-difference approximation, respectively. The formula is more accurate if N_f is large. In order to reduce the computational cost, N_f is chosen from 1 to 4, and yet, satisfactory results can still be obtained [16].

Let us consider the case of $N_f = 1$, for simplicity. When the supercell is divided into N grid points and isolated periodic boundary condition is imposed, the kinetic energy

operator can be rewritten as

$$-\frac{1}{2}\nabla^2\psi \approx -\frac{1}{2}\begin{pmatrix} c_0 & c_1 & 0 & 0 & \cdots & 0 & 0 \\ c_1 & c_0 & 0 & & & 0 & \\ 0 & \ddots & \ddots & \ddots & \ddots & & \vdots \\ \vdots & \ddots & c_1 & c_0 & c_1 & \ddots & \vdots \\ \vdots & & \ddots & \ddots & \ddots & \ddots & 0 \\ 0 & & & 0 & c_1 & c_0 & c_1 \\ 0 & 0 & \cdots & 0 & 0 & c_1 & c_0 \end{pmatrix}\begin{pmatrix} \psi(h) \\ \psi(2h) \\ \vdots \\ \psi(ih) \\ \vdots \\ \psi(Nh-h) \\ \psi(Nh) \end{pmatrix}, \tag{2.21}$$

where, $c_n = c_n^{(2)}$. If the periodic boundary condition is imposed, we have

$$-\frac{1}{2}\nabla^2\psi \approx -\frac{1}{2}\begin{pmatrix} c_0 & c_1 & 0 & 0 & \cdots & 0 & c_1e^{-ikL} \\ c_1 & c_0 & 0 & & & 0 & \\ 0 & \ddots & \ddots & \ddots & \ddots & & \vdots \\ \vdots & \ddots & c_1 & c_0 & c_1 & \ddots & \vdots \\ \vdots & & \ddots & \ddots & \ddots & \ddots & 0 \\ 0 & & & 0 & c_1 & c_0 & c_1 \\ c_1e^{ikL} & 0 & \cdots & 0 & 0 & c_1 & c_0 \end{pmatrix}\begin{pmatrix} \psi(h) \\ \psi(2h) \\ \vdots \\ \psi(ih) \\ \vdots \\ \psi(Nh-h) \\ \psi(Nh) \end{pmatrix}. \tag{2.22}$$

Here, k and L are the Bloch wave vector and the length of the supercell, respectively. The discretization of Kohn-Sham equation is now

$$-\frac{1}{2}\sum_{n=-N_f}^{N_f} c_n\psi(ih+nh) + \big(v_{ion}(ih) + v_H(ih) + v_{XC}(ih)\big)\psi(ih) = \epsilon\psi(ih). \tag{2.23}$$

The extension to higher-dimensional cases is straightforward.

2.3 Overbridging boundary-matching method

2.3.1 Ballistic transport and Landauer formula

The resistivity exists because an electron, while moving inside a crystal, is scattered by impurities, defects, or lattice vibrations. For a given material, an electron can acquire a mean free path, defined as the average length that the electron can travel freely without collision. The mean free path can be increased by reducing the number of impurities in a crystal or by lowering its temperature. When the mean free path of the electron is much longer than the dimension of the material through which the electron travels,

ballistic transport is realized, and the electron penetrates from one end to another. Ballistic conduction is typically observed in quasi-one-dimensional systems such as carbon nanotubes or metal nanowires.

To describe the basic theory of electrical transport through a quantum conductor, the Landauer formula is employed, which relates the conductance to the scattering properties of the conductor [17]. In its simplest form, where the systems has two terminals and the conductor has a single channel, the formula reads

$$G = \frac{2e^2}{h}\mathcal{T}, \tag{2.24}$$

where e is the electron charge, h is Planck's constant, and $\mathcal{T}$ is the transmission probability.

The formula can be extended to the case of multiple channels. Let t_{ij} be the probability amplitude at which electrons are transmitted from an initial mode j to a final mode i inside the conductor, we have the Landauer-Büttiker formula [17]

$$G = \frac{2e^2}{h}\sum_{i,j}|t_{ij}|^2\,\frac{v_i}{v_j}. \tag{2.25}$$

Here, v_j and v_i are the group velocities of the modes j and i, respectively.

2.3.2 Wave-function matching procedure

To study the electron-transport properties through a nanoscale junction, the whole system which includes the junction and semi-infinite electrodes, as shown in Fig. 2.2, needs to be treated. From the scattering theory, the scattering wave function corresponds to the solution of the Kohn-Sham equation of the whole system. The asymptotic form of the scattering wave function contains incident wave from the left electrode with the reflection to the left electrode and transmission to the right electrode. The global scattering wave is constructed under this asymptotic condition by matching the values of wave functions near the left and right boundaries of the electrodes, overbridging the transition region. This procedure is called overbridging boundary-matching method, and the detailed techniques can be found in Ref. [16].

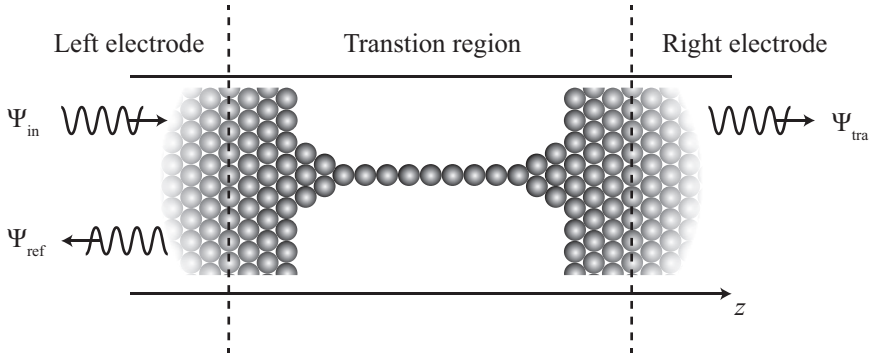

FIGURE 2.2: Schematic representation of the system with the transition region intervening between the left and right semi-infinite crystalline electrodes. In the left electrode, the incident wave and the reflected waves including evanescent ones are represented as Ψ_{in} and Ψ_{ref}, respectively, and in the right electrode, the propagating and decaying evanescent waves toward the right side are denoted by transmitted waves Ψ_{tra}.

2.4 Second-variation procedure and magnetic force theorem

2.4.1 Spin-orbit coupling

Spin-orbit coupling (SOC) is a relativistic effect, which can be derived from the Dirac equation following the approach in Ref. [18, 19]:

$$\left[\mathbf{p}^2 + \mathsf{V} + \mathbf{p}\left(\frac{1}{2\mathsf{M}} - 1\right)\mathbf{p} + \frac{i}{2}\boldsymbol{\sigma}\left(\frac{\mathbf{p}}{\mathsf{M}} \times \mathbf{p}\right)\right]\phi = \epsilon\phi, \tag{2.26}$$

with

$$\mathsf{M} = \frac{1}{2} + \frac{\epsilon - \mathsf{V}}{2c^2}, \mathsf{V} = V + \boldsymbol{\sigma}\mathbf{B}_{xc}. \tag{2.27}$$

Here, $\mathbf{p}$ is the momentum operator, V is the effective potential, ϵ is the eigenvalue, and $\boldsymbol{\sigma}$ is the spin operator, respectively. The first two terms in (2.26) correspond to the Hamiltonian in the Schrödinger equation, the third term corresponds to the scalar relativistic part, and the fourth term indicates SOC. Around the nucleus, central field approximation is assumed, i.e., $V(\mathbf{r}) = V(r)$, and by neglecting the spin polarization of the exchange-correlation potential $\mathbf{B}_{xc}((r))$, the SOC Hamiltonian is rewritten as

$$H_{soc} = \frac{i}{2}\boldsymbol{\sigma}\left(\frac{\mathbf{p}}{\mathsf{M}} \times \mathbf{p}\right) \approx -\frac{1}{2}\boldsymbol{\sigma}\left(\frac{1}{r}\frac{\mathrm{d}}{\mathrm{d}r}\left(\frac{1}{\mathsf{M}}\right)\mathbf{l}\right) \approx \frac{c^2}{(2c^2 + \epsilon - V)^2}\frac{1}{r}\frac{\mathrm{d}V}{\mathrm{d}r}\mathbf{l}\boldsymbol{\sigma}. \tag{2.28}$$

2.4.2 Second-variation procedure

The SOC mixes spin-up and spin-down states, resulting in spinor wavefunctions. Since SOC is a small effect and often does not have large influence on the density, second-variation procedure can be employed. In the second-variation procedure [20], each self-consistent iteration starts with a collinear magnetic density. In a first step, the Kohn-Sham equation is solved by neglecting the SOC, and in a second step, the full Hamiltonian including SOC is diagonalized in the subspace spanned by eigenfunctions in the first step. The advantage of the second-variation procedure is the physical transparency since it keeps spin as a good quantum number as far as possible, and the efficiency. The usage of this approach has been shown to obtain Δ_{SOC} which is in excellent agreement with experiments.

2.4.3 Magnetic force theorem

Since SOC is a small effect that has only a minor influence on the density, in many cases it is not necessary to include it in a selfconsistent calculation. Instead, one can use a potential from a selfconsistent calculation without SOC in order to construct the full Hamiltonian and diagonalize this Hamiltonian once. One application of this is the evaluation of magnetic anisotropy energy by the magnetic force theorem [21, 22]. According to this theorem, the magnetic moment of the system is first rotated and the magnetic anisotropy energy is calculated as the difference in sums of eigenvalues of occupied states.

To rotate the spin moment of the system with respect to the real-space crystal, in (2.28) ($\mathbf{l}\boldsymbol{\sigma}$) is replaced by $\mathrm{U}^{\dagger}(\mathbf{l}\boldsymbol{\sigma})\mathrm{U}$, where U is a spin rotation matrix.

$$\mathrm{U}(\vartheta,\varphi) = \begin{pmatrix} e^{-i\frac{\varphi}{2}}\cos(\frac{\vartheta}{2}) & -e^{-i\frac{\varphi}{2}}\sin(\frac{\vartheta}{2}) \\ e^{+i\frac{\varphi}{2}}\sin(\frac{\vartheta}{2}) & e^{+i\frac{\varphi}{2}}\cos(\frac{\vartheta}{2}) \end{pmatrix}, \tag{2.29}$$

where, ϑ and φ are the Euler's angles.

Chapter 3

Electronic Structures and Magnetic Anisotropy Energies of Graphene with Adsorbed Transition-Metal Adatoms

3.1 Introduction

Graphene is a two-dimensional honeycomb lattice of carbon atoms that has attracted great interest both theoretically and experimentally. Owing to its high carrier mobility and weak spin-orbit coupling (SOC), graphene is considered as a promising material for spintronic devices. For the design of semiconductor devices, there are some problems of graphene that need to be overcome. In the absence of SOC, graphene is a zero-gap semiconductor with the Dirac cone structure at the Fermi level. The conversion of graphene to an insulator is highly desirable. In addition, since a pristine graphene is also known to be nonmagnetic, external methods are needed to magnetize a graphene. Thus, it is difficult to tune the electronic structures of graphene while simultaneously realize the desired spin texture.

Recently, scanning tunneling microscopy measurement conducted by Gyamfi *et al.* [23] confirmed that it is possible to deposit single transition-metal atoms on a monolayer graphene. Such systems are of particular interest because transition-metal atoms can magnetize graphene and open a gap at the Dirac point through SOC [24]. Experimentally, Eelbo *et al.* found that Fe and Co adatoms on graphene exhibit an out-of-plane easy magnetization axis [25]. On the theoretical side, the magnetic anisotropy energies

(MAEs) obtained by fully relativistic calculations using DFT indicated the existence of an out-of-plane easy axis for the Co adatom but an in-plane easy axis for the Fe adatom [26]. Another DFT study using the projector augmented-wave method also revealed that the Fe adatom on graphene exhibits an in-plane easy axis [27]. Although the magnetic moment of the Co adatom computed by DFT calculations is consistent with that obtained experimentally, there appears to be a contradiction in the case of the Fe adatom. The DFT calculations contain some artifacts or do not provide sufficient results, which prevents us from discussing the discrepancy with the experimental result: the calculations in Ref. [26] only relax the positions of the adatoms and their first-nearest-neighbor carbon atoms, and Ref. [27] is entirely focused on the case of the Fe adatom. Studies on the MAEs of metal atoms on graphene systems are limited and there still remains much to be learned about the magnetic moments of transition metals on graphene.

In this chapter, I investigate the electronic structures of graphene adsorbed with an Fe, Co, or Ni adatom in the presence of SOC, and evaluate their MAEs for different magnetization directions by DFT calculations. Structural optimization is performed for all atoms in the supercell. My results show that energy gaps are opened at the crossing points of spin-up and spin-down bands near the Dirac point in the cases of Fe and Co adatoms as a result of SOC. The Rashba effect is realized in the case of the Ni adatom, resulting in a $\mathbf{k}$-dependent energy shift of the π bands at the bottom of the Fermi surface. The Co adatom exhibits an out-of-plane easy axis, while the Fe adatom shows the in-plane easy magnetic orientation, in agreement with previous DFT calculations [26, 27].

3.2 Computational models

The first-principles calculations are performed within the framework of DFT using the real-space finite-difference approach [15], which enables us to determine the self-consistent electronic ground state with a high degree of accuracy using a time-saving double-grid technique [16, 28–30]. The electron-ion interaction is described using the projector augmented-wave method [31], and the exchange-correlation interaction is treated within the local spin density approximation [32]. The SOC is calculated by a second-variation procedure [20] and the MAE is calculated by the magnetic force theorem [21, 22].

Figure 3.1(a) shows the computational model of the system comprising a metal atom on graphene. I employ tetragonal supercells, in which periodic boundary conditions are imposed in all directions. A grid spacing of 0.21 Å is used and a grid of $8 \times 8 \times 1$ points in the irreducible Brillouin zone is employed. The directions between the symmetry points

defined in Fig. 3.1(b) are used to plot the band structures. The carbon-carbon distance is chosen as 1.42 Å, and the transition-metal adatom is situated on one of the hollow sites of graphene, which is known to be the most favorable configuration [25, 33–41]. A vacuum of 15 Å is inserted between the periodic images of graphene sheets to avoid spurious interactions. All atoms are allowed to relax until all remaining forces are less than 0.05 eV/Å. After structural optimization, I found that the second-nearest-neighbor carbon atoms to the adatoms move by as much as 0.1 Å.

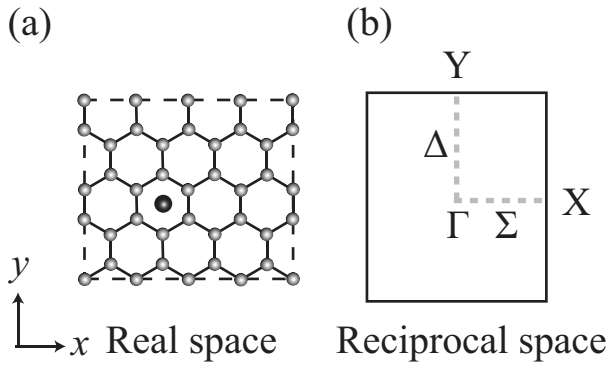

FIGURE 3.1: (a) Computational model of graphene adsorbed with transition-metal adatom in real space and (b) Brillouin zone in reciprocal space with notation of symmetry points and symmetry lines. Black and white spheres indicate metal and carbon atoms, respectively, and the broken rectangular denotes the supercell.

3.3 Results and discussion

3.3.1 Band structure analysis

Figure 3.2 plots the electronic band structure of the systems with different metal atoms on graphene. The electronic structure is spin-polarized in the case of Fe or Co adsorption, while it is not in the case of Ni adsorption. The spin polarizations of Fe and Co adatoms are found to be 2.0 and 1.0 μ_B, respectively. One can see that the magnetizations of the adatoms are greatly reduced compared with those of the isolated atoms. This is explained by the promotion mechanism [23, 42], in which two electrons are transferred from the $4s$-orbitals to the $3d$-orbitals of the metal adatoms.

An important feature that can be seen in the band structures is a clear linear dispersion at the Dirac point around the Fermi level. It is notable that the Dirac point is only well defined for the spin-up band in the case of Fe adsorption. In the case of Co adsorption, four crossing points arise from the relative shift between the spin-up and spin-down bands around the Dirac point. For the case of Ni adsorption, owing to the vanishing magnetic moment, the band structure at the Dirac point is unaffected by the adatom

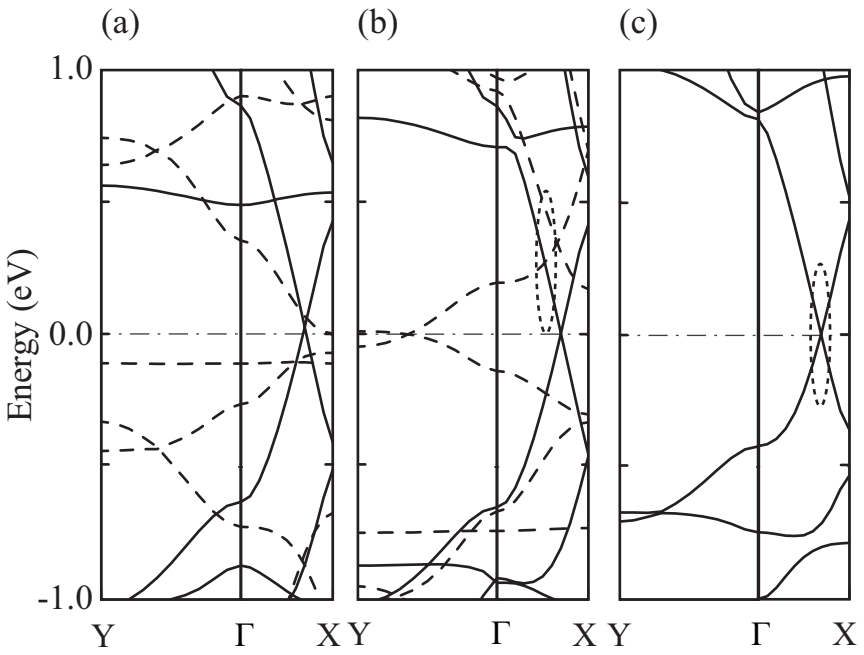

FIGURE 3.2: Band structures of graphene adsorbed with (a) Fe, (b) Co, and (c) Ni adatoms. The solid (dashed) curves indicates spin-up (spin-down) electronic bands. Zero energy is taken to be the Fermi level, which is represented by dashed-dotted lines.

compared with that of a pristine graphene, in agreement with previous DFT calculations [34].

Figure 3.3 shows enlargements of the band structures near the crossing points between the spin-up and spin-down bands around the Dirac point for Co and Ni adsorption, which are denoted by the dotted circles in Fig. 3.2. The band gap is opened at the crossing point owing to the presence of SOC as shown in Fig. 3.3(b). The gap is found to be 15 meV for the case of Co adsorption. When a metal adatom is placed on a graphene, a sizable potential gradient is formed at the interface, inducing a considerable SOC. Although the induced SOC and magnetization in graphene are nonuniformly distributed, the gap-opening mechanism near the Dirac point is the same as that proposed in the tight-binding model with uniformly distributed SOC and magnetization [24]. The spin-up (spin-down) bands are shifted upward (downward), leading to the band crossing, and the SOC lifts the spin degeneracy at the band crossing points, thus opening energy gaps. Although the gap is not opened for Ni adsorption, the SOC at the Dirac point of 20 meV is quite large compared to that of 25×10^{-3} meV for the pristine graphene [43]. Figure 3.4 shows the projected density of states of graphene with adsorbed Ni adatom onto metal atomic orbitals. In the vicinity of the Fermi level, there are some contribution of Ni d bands. Thus, the increase in the SOC is attributed to the hybridization between carbon π bands and Ni d bands, and to the transverse electric field induced by the asymmetry of the adatom-graphene structure [43]. Additionally, I found a linear $\mathbf{k}$-dependent energy shift

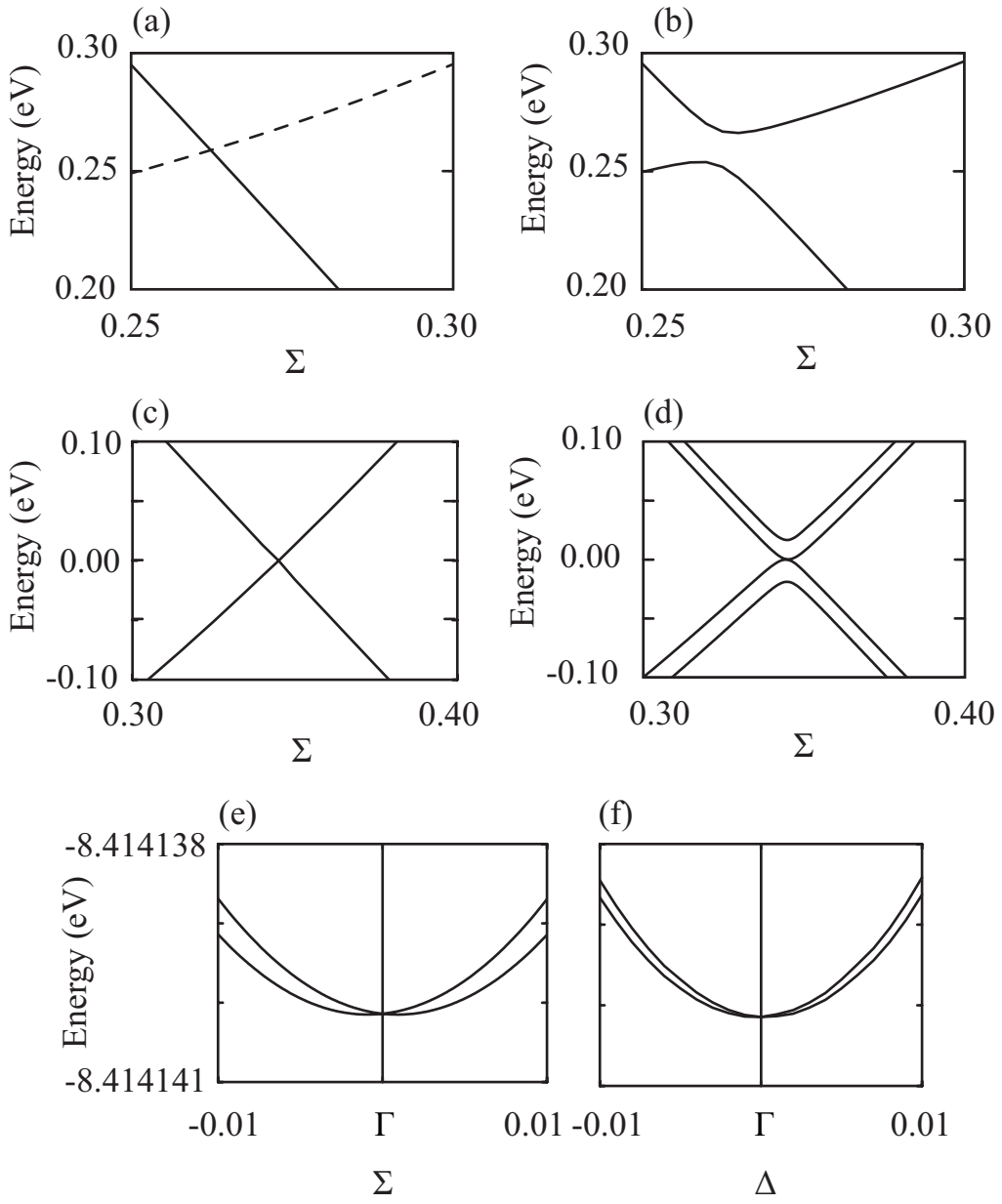

FIGURE 3.3: Band structures near Dirac point denoted by dotted circles in Fig. 3.2 for Co adsorption in the (a) absence and (b) presence of SOC, and for Ni adsorption in the (c) absence and (d) presence of SOC. Band structures near the bottom of the Fermi surface of the π bands in the presence of SOC along the (e) x- and (f) y-directions. The values on the horizontal axes are in the units of π/L_x and π/L_y, where L_x and L_y are the lengths of the supercell in the x- and y-directions, respectively.

at the bottom of the Fermi surface of π bands, at around –8.41 eV in the case of Ni adsorption, as shown in Figs. 3.3(e) and 3.3(f). The shifting of the bands is attributed to the manifestation of the Rashba effect.

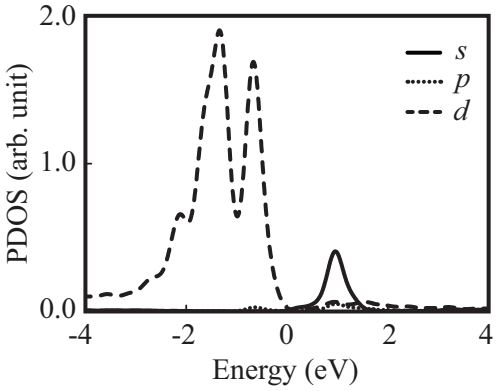

FIGURE 3.4: Projected density of states onto metal atomic orbitals of graphene adsorbed with Ni adatom. The zero energy is taken to be the Fermi level.

3.3.2 Magnetic anisotropy energies

In the absence of SOC, the magnetic moments of all electrons are parallel or antiparallel to one axis and the total energy is independent of the direction of the magnetic moments. When SOC is included, this rotational symmetry is broken and the energy of a system depends on the direction of the magnetization axis. To evaluate the MAE of a system comprising a metal atom on graphene, the magnetization direction is rotated and the sums of the eigenvalues of occupied states $\mathrm{E}(\theta, \phi)$, where θ and ϕ are the usual polar and azimuthal angles of the spin measured from the z- and x-directions, respectively, are calculated.

Figure 3.5 shows the calculated MAEs for different in-plane angles ϕ. The dependence of the in-plane MAE curves on the in-plane angle ϕ closely follows the $\cos^2\phi - \sin^2\phi$ function, which is attributed to the use of rectangular supercells and to the excitations of a spin in an anisotropic environment [27, 44]. It can be seen that the Fe adatom exhibits an in-plane easy axis with an MAE of 1.6 meV. The Co adatom exhibits an out-of-plane easy magnetization axis with an MAE of 5.6 meV. My findings are in reasonable agreement with previous theoretical MAE calculations [26, 27]. By x-ray magnetic circular dichroism measurement, Eelbo *et al.* found that both Fe and Co adatoms exhibit an out-of-plane easy axis [25]. My calculations qualitatively support the results of their experiments in the case of a Co adatom, and contradict them in the case of an Fe adatom.

Figure 3.6 plots the projected density of states of graphene adsorbed with Fe and Co adatoms onto metal atomic orbitals. The interaction between the graphene and the transition-metal adatoms splits the five-fold degenerate $3d$-orbitals of the metal atoms

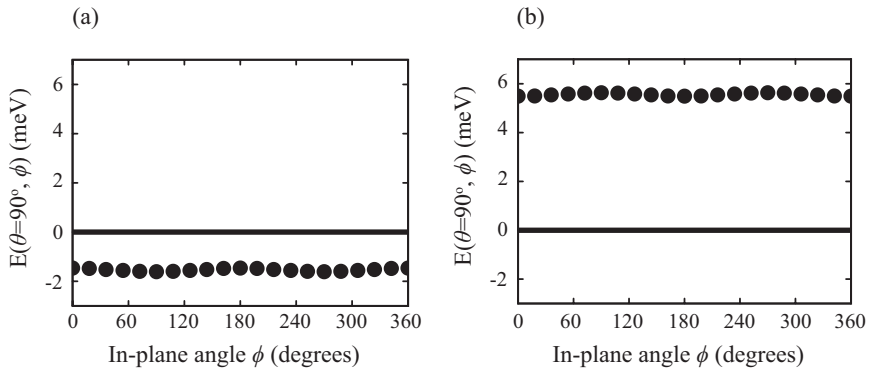

FIGURE 3.5: Dependence of E(θ=90°, ϕ) on in-plane angle ϕ for (a) Fe and (b) Co adatoms on graphene. The energy E(θ=0°, ϕ=0°) is taken as zero energy.

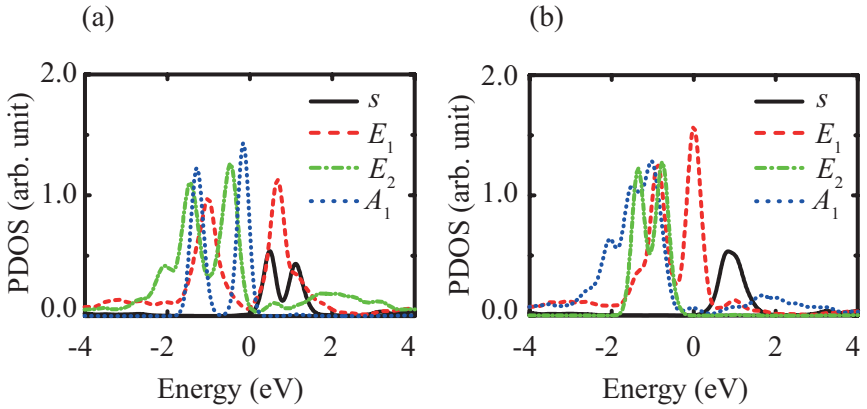

FIGURE 3.6: Projected density of states onto metal atomic orbitals of graphene adsorbed with (a) Fe and (b) Co adatoms. The zero energy is taken to be the Fermi level.

in two-fold degenerate E_1 orbitals (which contain d_{xz} and d_{yz} orbitals), another two-fold degenerate E_2 orbitals (which contain d_{xy} and $d_{x^2-y^2}$ orbitals), and a single-fold A_1 orbital (which contain d_{z^2} orbital).

From Section 2, we know that

$$\mathcal{H}_{soc} \sim \mathbf{l}\boldsymbol{\sigma} = l_z\sigma_z + \frac{l_+\sigma_- + l_-\sigma_+}{2}. \tag{3.1}$$

The SOC Hamiltonian can be divided into perpendicular part $\mathcal{H}^{\perp}_{soc} \sim l_z\sigma_z$ and parallel part $\mathcal{H}^{\parallel}_{soc} \sim \frac{l_+\sigma_- + l_-\sigma_+}{2}$. The MAE is defined as:

$$E_{MAE} = \langle\psi|\mathcal{H}^{\parallel}|\psi\rangle - \langle\psi|\mathcal{H}^{\perp}|\psi\rangle = \langle\psi|\mathcal{H}^{\parallel}_{soc}|\psi\rangle - \langle\psi|\mathcal{H}^{\perp}_{soc}|\psi\rangle, \tag{3.2}$$

where, $\mathcal{H}^{\parallel}$, $\mathcal{H}^{\perp}$, $\mathcal{H}^{\parallel}_{soc}$, and $\mathcal{H}^{\perp}_{soc}$ are the total Hamiltonian and SOC Hamiltonian for parallel and perpendicular magnetic moment, respectively, and ψ is the wave function.

Since $\langle d_{xz}|l_z\sigma_z|d_{yz}\rangle \neq 0, \langle d_{xz}|l_+\sigma_-|d_{yz}\rangle = \langle d_{xz}|l_-\sigma_+|d_{yz}\rangle = 0$, and SOC mixes the two-fold degenerate states with E_1 character into $\psi_\pm$ states, we have

$$\langle \psi_\pm|\mathcal{H}_{soc}^{\parallel}|\psi_\pm\rangle = 0, \langle \psi_\pm|\mathcal{H}_{soc}^{\perp}|\psi_\pm\rangle = \pm a. \tag{3.3}$$

Thus, the occupation of E_1 orbitals is important to determine the magnetic anosipotry. In the case of Co adsorption, the E_1 orbitals are occupied and the Co adatom on graphene favors the out-of-plane magnetic orientation. The E_1 orbitals are unoccupied in the case of Fe adsorption, resulting in an in-plane magnetization axis. The discrepancy with the experimental result in the case of an Fe adatom can be attributed to the fact that in experiments electrons may originate from the substrate and migrate to the graphene [45], giving rise to the out-of-plane easy magnetization axis.

3.4 Summary

I have studied the electronic structures and MAEs of graphene with an adsorbed Fe, Co, or Ni adatom by first-principles calculations using DFT. Energy gaps are opened at the crossing points of spin-up and spin-down bands near the Dirac point as a result of SOC in the case of adsorption with Fe and Co adatoms. A **k**-dependent energy shift of the π bands is observed at the bottom of the Fermi surface, indicating the presence of the Rashba effect in the case of Ni adsorption. The calculated MAEs show that the Co adatom exhibits an out-of-plane easy axis, in agreement with experimental results, whereas the Fe adatom favors the in-plane magnetization axis, in contrast with experimental observations. It was found that the occupation of E_1 orbitals is important for magnetic anisotropy in the cases of Fe and Co adsorption. These results are expected to stimulate interest in the use of these materials in spintronic applications.

Chapter 4

Electronic Structures and Electron-Transport Properties of Carbon/Boron Nitride Nanotubes

4.1 Introduction

4.1.1 Edge states and magnetism

4.1.1.1 Carbon and boron-nitride nanoflakes

Honeycomb nanostructures of carbon have attracted considerable interest owing to their interesting electronic and magnetic properties that can be applied in future electronic and spintronic devices. In these nanostructures, localized edge states are observed at the zigzag edges of carbon giving rise to the local magnetism and governing the spin-dependent transport. In 1996, Fujita *et al.* [46] studied the electronic states of armchair and zigzag graphene nanoribbons and they found peculiar electronic states which are localized at the zigzag boundaries of a zigzag graphene nanoribbon (ZGNR). These states show a remarkably sharp peak in density of states (DOS) at the Fermi level, which does not emerge in the case of a pristine graphene. Figure 4.1 shows the geometry of a ZGNR. Following the tight-binding approach given by Kohmoto and Hasegawa [47], we can derive an analytic solution for the edge states:

$$\begin{aligned} \psi_{L_x-n} &= (-t^{2n+1/2})\psi_{L_x+1/2} \\ \phi_n &= (-t)^{2n-1}\phi_{1/2} \end{aligned} . \tag{4.1}$$

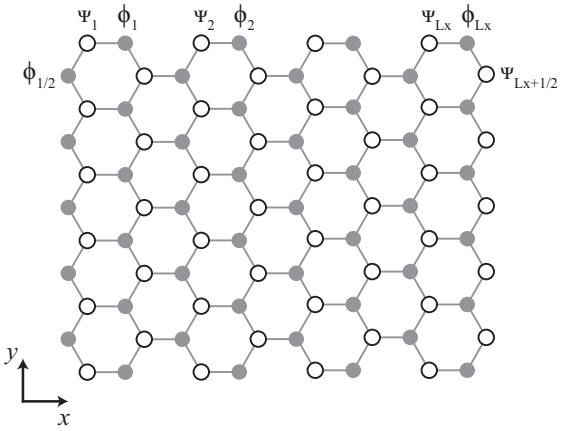

FIGURE 4.1: Ball-and-stick model of a ZGNR with periodicity imposed in the y-direction.

Thus, the wave functions ϕ_n and ψ_n are coupled, and the edge states are localized at the zigzag edges with the localization length

$$\xi = \frac{1}{2|\log t|}, \tag{4.2}$$

where

$$t = \sqrt{2(1+\cos k_y)} = 2\left|\cos\frac{k_y}{2}\right|. \tag{4.3}$$

The zero-mode edge states are observed if $t > 0$ or $|k_{\mathrm{y}}| > \frac{2\pi}{3}$, where k_{y} is the reciprocal lattice vector in the y-direction.

Since the DOS at the Fermi level is large, the presence of the edge states should induce spontaneous magnetism. The edge state at one side of the ZGNR consists of mainly spin-up electrons, and the edge state on the opposite side comprises of mainly spin-down electrons, leading to a ferrimagnetic spin structure [46, 48].

When studying hexagonal carbon/boron-nitride (h-CBN) nanoflakes, Ono *et al.* [1] found spin-polarized edge states at the zigzag edges of carbon segments (see Fig. 4.2(a)). The spin polarization here is attributed to the manifestation of Lieb's theorem for a bipartite lattice, which states that the itinerant magnetism is equal to $N_A - N_B$, where N_A (N_B) is the number of atoms on the A (B) site [49]. They also revealed that these h-CBN nanoflakes with a localized magnetic moment along their zigzag edges of carbon exhibit spin-dependent transport behavior (see Fig. 4.2(c)). Since the magnetic properties of the honeycomb nanostructures of carbon are highly dependent on their size and edge shapes, the formation of spin-polarized edge states is the key mechanism to achieve spin-dependent transport. From the experimental viewpoint, the fabrication of such h-CBN has been realized by high resolution transmission electron microscopy measurement [2] (see Fig. 4.3). In addition, it has been predicted that the carbon and

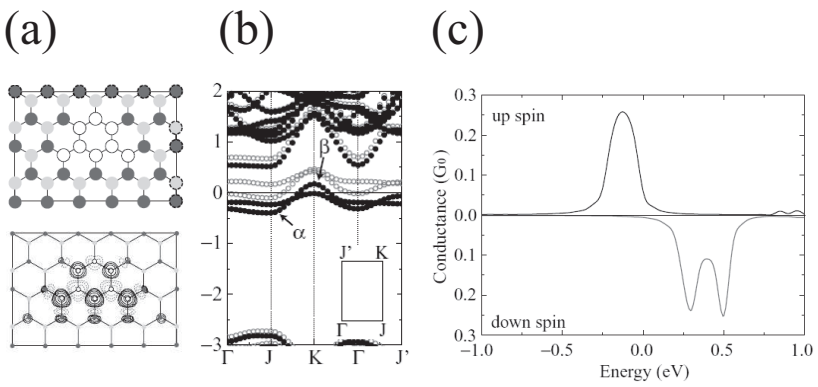

FIGURE 4.2: (a) Computational model of a h-CBN nanoflake and isocontour of edge states. White, black, and grey circles represent carbon, boron, and nitrogen atoms, respectively. (b) Electronic band structure of the h-CBN nanoflake. Black and white dots indicate spin-up and -down states, respectively.(c) Conductance as function of incident energy of electrons of the h-CBN nanoflake. Figure is taken and modified from Ref. [1]

boron-nitride domains tend to segregate and form isolated islands in the thermodynamics limits [50]. Thus, the applications of the edge states to the field of spintronics is very promising.

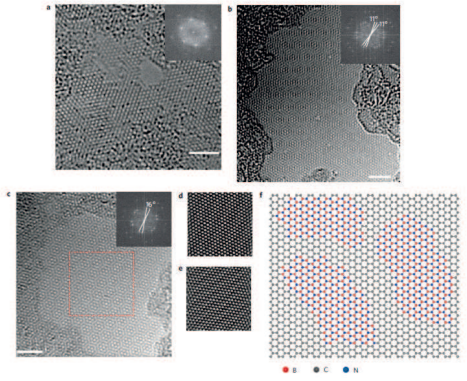

FIGURE 4.3: From **a** to **e**, High resolution transmission electron microscopy images and **f** atomic model of a h-CBN film showing hybridized carbon and boron-nitride domains. Figure is taken from Ref. [2].

4.1.1.2 Carbon and boron-nitride nanotubes

The edge states can also be observed in a zigzag carbon nanotube (CNT), which is considered as a rolled up graphene. If one assigns two primitive lattice vectors on a graphene sheet $\mathbf{R}_1$ and $\mathbf{R}_2$, then any point on the honeycomb lattice can be expressed by $\mathbf{R} = n\mathbf{R}_1 + m\mathbf{R}_2$, i.e., by a pair of integers (n,m). The CNT is formed by rolling up the graphene from the origin to the point $\mathbf{R}$ along the cylinder circumference. The pair of integer (n,m) is called chirality of the CNT.

Using tight-binding model, it was shown that:

+ If $n = m$, the CNT is a metal.

+ If $n - m = 3q$ and q is an integer different from 0 (zigzag nanotube), the CNT is a narrow-gap semiconductor.

+ If $n - m \neq 3q$, the CNT is a moderate-gap semiconductor.

The electronic structure of a CNT can be derived from that of a graphene by imposing the periodicity along the nanotube circumference [51]. It was found by Okada and Oshiyama that the existence of the edge states in a zigzag CNT is a direct consequence of rolling up a ZGNR into the nanotube [52]. Nevertheless, spin polarization and spin-dependent transport utilizing the edge states cannot be achieved straightforwardly as in the case of graphene because there is little freedom in exchanging atoms between A and B sites owing to the periodicity along the circumference of CNTs. First-principles studies carried out by Choi *et al.* [53] demonstrated that the alternate placement of zigzag CNTs and zigzag boron-nitride nanotubes (BNNTs), which are possibly fabricated by the laser vaporization method [3] (see Fig. 4.4), resulted in magnetic ordering by doping electrons or holes, and they found that the magnetic ground states are associated with the zigzag edges of CNTs. Such systems are of interest for the applications of spintronic devices. However, electron or hole doping is not practical when the structure is connected to electrodes because carriers enter the nanotube and spin polarization is not retained. In addition, the rotational symmetry mismatch between the conducting and edge states of a zigzag CNT with respect to the nanotube axis prevents electron transport; for example, conducting states with 3-fold rotational symmetry are hardly connected to edge states with 5-fold symmetry in the case of a (9,0) CNT [4]. This symmetry mismatch problem will be discussed in the next section.

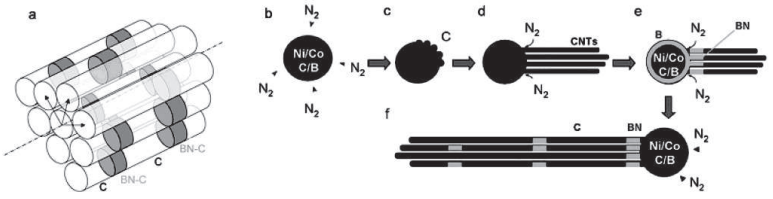

FIGURE 4.4: From **a** to **f**, Sequential growth showing a longitudinal segregation of carbon and boron-nitride nanotubes. Figure is taken from Ref. [3].

4.1.2 Electron transport through edge states

In the electron transport through a junction formed a finite length CNT connected to CNT electrodes of different chirality, conductance gap is observed when the finite length CNT and the CNT electrodes have different rotational symmetry. The discrete levels in the finite length CNT do not couple to the leads continua, and thus, do not transfer any current [54]. Ono *et al.* investigated the electron transport through a junction formed by CNT and BNNT and they found that the conductance is suppressed because the edge states with 5-fold rotational symmetry are hardly connected to the CNT states with 3-fold symmetry [4] (see Fig. 4.5). Therefore, the spin-dependent transport property of

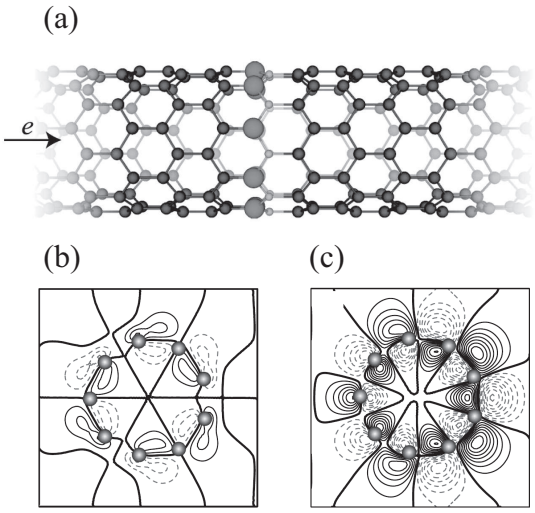

FIGURE 4.5: (a) Computational model of a BNNT suspended between semi-infinite CNT electrodes. Black, large grey, and small white circles represents carbon, boron, and nitrogen atoms, respectively. Charge density of (b) conducting CNT states and (c) edge states in the plane perpendicular to the nanotube axis. Figure is taken and modified from Ref. [4].

the heterojunction between zigzag CNT and BNNT suspended by CNT electrodes has not been investigated so far, although CNTs are the most natural option for electrodes.

In this chapter, the electronic structures and electron-transport properties of the heterojunction between carbon/boron-nitride nanotubes, in which CNTs are sandwiched between BNNTs along the tube axis, are studied by first-principles calculations based on DFT. Instead of electron or hole doping, I propose the atom substitutional doping, in which, e.g., one N atom is replaced with one C atom at the zigzag CNT edge. It is found that the spin polarization is realized due to the variation of the occupation number of the energetically flat edge states by the p-type atom substitutional doping. On the other hand, in the case of n-type doping, the σ-π hybridization of the smaller-diameter nanotubes due to the small curvature pulls down the energetically dispersive states, which results in the nonmagnetic ground-state electronic structure, while the spin

polarization is realized in larger-diameter nanotubes. More interestingly, in contrast to the undoped nanotube, where the electron transport through the edge states is not permitted owing to the symmetry mismatch between the edge states and conducting CNT states, the fluctuation of the symmetry due to the presence of the doped atom leads to the spin-dependent resonant tunneling through the edge states.

4.2 Computational models

The first-principles calculations are performed within the framework of DFT using the real-space finite-difference approach [15], which enables us to determine the self-consistent electronic ground state with a high degree of accuracy using a time-saving double-grid technique [16, 28–30]. The electron-ion interaction is described using norm-conserving pseudopotentials NCPS97 [55] generated by the scheme proposed by Troullier and Martins [12], and the exchange-correlation interaction is treated within the local spin density approximation [56].

I study a number of carbon/boron-nitride nanotubes by varying the compositions of carbon and boron-nitride segments of tube. Each nanotube is denoted by $C_i(BN)_j$, in which i and j indicate the number of carbon and boron-nitride rings in a supercell, respectively. Figure. 4.6 shows the computational model of $C_i(BN)_j$ nanotubes, in which CNT has zigzag or bearded edges, and shall be referred from now on by a prefix *z*- or *b*-. Tetragonal supercells are adopted under periodic boundary conditions in all directions. The wall-to-wall distance between adjacent nanotubes is chosen so as to exceed 6 Å, which permits the neglection of tube-tube interactions. A grid spacing of 0.17 Å is used and a sufficiently dense grid in the irreducible Brillouin zone is employed. Only the lattice constant of the CNT is relaxed and structural optimizations for the other nanotubes are performed until the remaining forces are less than 0.05 eV/Å under the lattice constant of the CNT.

Since the primary importance is attached to the magnetic moment of the carbon/boron-nitride nanotube, the occupation of the zigzag CNT edge states is crucial for the spin polarization. When a short BNNT is simply connected to semi-infinite CNT electrodes, the injected holes by the substitution will be filled with electrons from the nearby C atoms in the electrodes. Hence, the model, in which a short inner CNT is connected at both its ends to the BNNTs and all of these components intervene between the outer CNTs, is employed as shown in Fig. 4.7. Here and hereafter, I refer to this transport model as CBNNT.

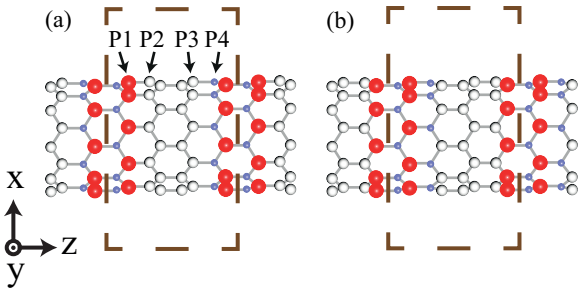

FIGURE 4.6: Computational model of a (9,0) (a) z-$C_2(BN)_2$ and (b) b-$C_2(BN)_2$. White, light blue (grey), and red (black) balls are C, N, and B atoms, respectively. P1, P2, P3, and P4 indicate positions at which one B atom is replaced with one C atom, one C atom is replaced with one N atom, one C atom is replaced with one B atom, and one N atom is replaced with one C atom, respectively. The rectangles enclosed by dashed lines represent the supercells.

The electron-transport property of the CBNNT is computed using scattering wave functions continuing from one electrode to the other, which are obtained by the overbridging boundary-matching method [16, 57]. The Kohn-Sham effective potential in the scattering region is first calculated under the periodic boundary conditions, and then the wave functions are obtained non-self-consistently. It has been reported that this procedure is as accurate as fully self-consistent calculations in the linear response regime and significantly more efficient than carrying out calculations self-consistently on a scattering basis [58]. A grid spacing of 0.23 Å is employed and the Brillouin zone for the scattering region containing 144 atoms is sampled by 4 k-points along the tube axis to set up the Kohn-Sham effective potential. The conductance under zero temperature and zero bias is described by the Landauer-Büttiker formula [59], $G = G_0 \sum_{i,j} |t_{ij}|^2 \frac{v_i}{v_j}$, where t_{ij} is the transmission coefficient at which electrons are transmitted from an initial mode j to a final mode i inside the scattering region, v_i and v_j are the longitudinal components of the group velocity in modes i and j, $G_0 = e^2/h$, with e and h being the electron charge and Planck's constant, respectively.

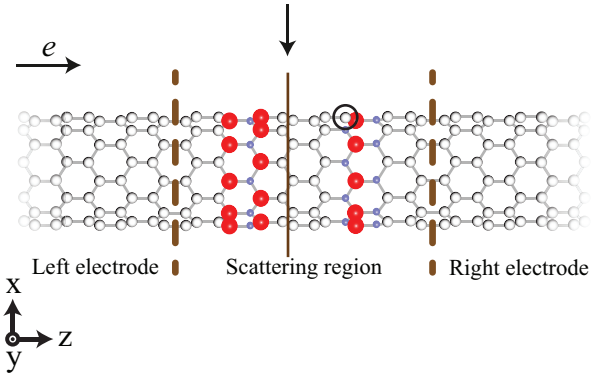

FIGURE 4.7: Computational model of CBNNT suspended between semi-infinite CNT electrodes. The circle indicates the position at which one N atom is replaced with one C atom. Meaning of symbols are the same with those in Figure 4.6.

4.3 Results and discussion

4.3.1 Undoped carbon/boron-nitride nanotube

The electronic band structures of the CNT, z-$C_2(BN)_2$ and b-$C_2(BN)_2$ are shown in Figs. 4.8(a), 4.8(b), and 4.8(c), respectively. The (9,0) CNT has a small band gap, which agrees with the results of a previous experiment [60] and theoretical studies [61]. On the other hand, BNNTs are semiconductors with a large band gap attributed to their ionic bonding [62]. The carbon/boron-nitride nanotubes exhibit energy gaps of 1.0 eV as a result of the confinement of the CNT segment in a finite area.

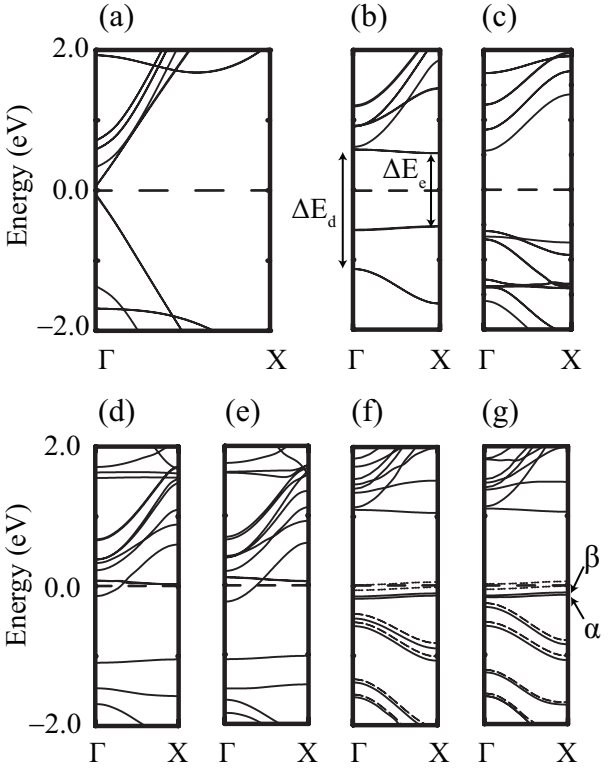

FIGURE 4.8: Band structures of (a) (9,0) CNT, (b) z-$C_2(BN)_2$, and (c) b-$C_2(BN)_2$. (d), (e), (f), and (g) show the band structures of doped C/BN nanotubes in which one B atom is replaced with one C atom, one C atom is replaced with one N atom, one C atom is replaced with one B atom, and one N atom is replaced with one C atom, respectively. Zero energy was chosen as the Fermi level. Solid (dashed) curves indicate the spin-up (-down) states.

An important feature found in the band structure of the z-$C_2(BN)_2$ is the occurrence of nearly dispersionless bands, which are doubly degenerate, around the Fermi level. The charge density distributions of the flat bands decay exponentially toward the center of the CNT and BNNT. In addition, the occupied (unoccupied) flat bands are associated with the C-B bonding (C-N antibonding) states with the majority of the charge density located at C atoms. The charge density distribution of one occupied (unoccupied)

edge state is localized along one half of a zigzag CNT edge and that of the remaining occupied (unoccupied) edge state is aligned along the other half of the zigzag CNT edge, indicating the presence of the spontaneous symmetry breaking [63]. When a truncated zigzag CNT is connected to BNNTs, the energy of the edge state is determined by the hybridization between two p_z orbitals of edge atoms. The hybridization between C and B (N) p_z orbitals forms C-B (C-N) bonding and antibonding states. The C-B bonding (C-N antibonding) state lies close to the Fermi level while the C-B antibonding (C-N bonding) state locates far from the Fermi level as shown in Fig. 4.9, resulting in that the C-B bonding (C-N antibonding) state is occupied (unoccupied). On the other hand, the C-B and C-N bonds at the boundary of the z-$C_2(BN)_2$ are replaced by the C-C and B-N bonds in the case of the b-C/BNNT. Because the splitting of the C-C (B-N) bonding and antibonding states due to the hybridization is larger than the energy difference between the C-B bonding and C-N antibonding state, the edge states are not observed near the Fermi level in the b-$C_2(BN)_2$.

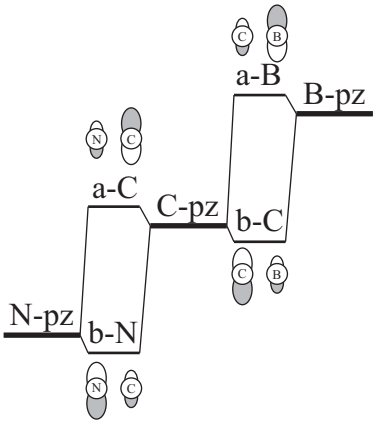

FIGURE 4.9: Schematic of the energy diagram for the formation of the edge states.

It is of interest to examine how the energies of the edge states change with respect to the length of the CNT and BNNT. Figure 4.10 shows the energy difference between occupied and unoccupied edge states, indicated by ΔE_e as seen in Fig. 4.8, as a function of the CNT length. One can see that, ΔE decreases when the length of the CNT increases or the length of the BNNT decreases. In addition, for a fixed BNNT length, ΔE quickly converges to a constant when the length of the CNT is increased, which is attributed to the charge transfer from C-N bonds to C-B bonds.

As shall be shown later, the relative position between the edge and dispersive states is essential to determine the spin polarization in doped carbon/boron-nitride nanotubes. Table 4.1 summaries the energy differences between occupied and unoccupied states for the edge states and dispersive states, which are closest to the Fermi level. When the length of the BNNT is long, the edge states are HOMOs and LUMOs up to very long CNT. For a sufficiently long BNNT, ΔE is smaller than the band gap of CNT, e.g.,

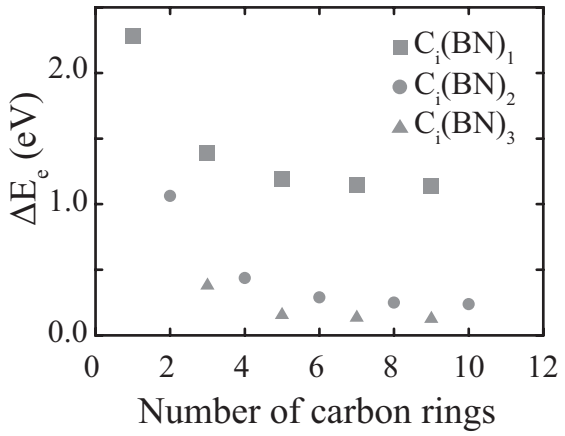

FIGURE 4.10: Dependence of ΔE on the length of the CNT.

TABLE 4.1: Energy differences between occupied and unoccupied edge states ΔE_e, and those between occupied and unoccupied dispersive states closest to the Fermi level ΔE_d, as functions of length of CNT. The unit for energy is eV.

$(BN)_1$	ΔE_e	ΔE_d
$C_1(BN)_1$	2.279	2.033
$C_3(BN)_1$	1.392	1.006
$C_5(BN)_1$	1.193	0.666
$C_7(BN)_1$	1.149	0.527
$C_9(BN)_1$	1.140	0.428
$(BN)_2$	ΔE_e	ΔE_d
$C_2(BN)_2$	1.064	1.795
$C_4(BN)_2$	0.438	1.163
$C_6(BN)_2$	0.291	0.841
$C_8(BN)_2$	0.251	0.663
$C_{10}(BN)_2$	0.239	0.550
$(BN)_3$	ΔE_e	ΔE_d
$C_3(BN)_3$	1.064	1.795
$C_5(BN)_3$	0.438	1.163
$C_7(BN)_3$	0.291	0.841
$C_9(BN)_3$	0.251	0.663

ΔE of a $C_7(BN)_5$ is 77 meV. Thus, the length of BNNT can be adjusted to tune the electronic structures of the carbon/boron-nitride nanotubes.

4.3.2 Doped carbon/boron-nitride nanotube

Since the edge states in the z-$C_2(BN)_2$ induce a large density of states closest to the Fermi level, inserting or removing electrons causes spin polarization according to the Stoner criterion [64, 65]. However, electron or hole doping is not preferable in practice because carriers enter the nanotube when the z-$C_2(BN)_2$ is connected to semi-infinite CNT electrodes and the system is not spin-polarized. I propose the alternative method of

atom substitutional doping, in which one C atom at the CNT/BNNT interface is replaced with one B (N) atom or vice versa as shown in Fig. 4.7(a) so that spin polarization can be induced and retained when the nanotube is connected to the electrodes. Furthermore, I found that the formation energy of atom substitution at the CNT/BNNT interface is less than that in a pure CNT by 1.2 eV and 1.0 eV for B and N atom substitution, respectively. This result indicates that atom substitution preferentially occurs at the CNT/BNNT interface.

As shown in Fig. 4.7, p-type substitutional doping favors spin polarization and the degeneracy of the edge states is broken: In the vicinity of the Fermi level, one down-spin edge state is occupied and the other down-spin edge state is unoccupied resulting in a spin-polarized electronic structure with a magnetic moment of $1\mu_B$ per supercell. On the contrary, n-type substitutional doping does not lead to the magnetic ground-state electronic structure. This behavior can be interpreted in terms of the band structure of the z-$C_2(BN)_2$. When a hole is doped into the system (p-type doping), the Fermi level is aligned with the valence band maximum and the Coulomb energy of the doped bands decreases. If the edge states are the valence band maximum, then spin polarization is induced (see Fig. 4.11(a)). On the other hand, if the occupied dispersive states, which lie below the edge states in the undoped case, cross the Fermi level, an electron will be taken from the dispersive states, resulting in the nonmagnetic ground state. Figure 4.11(b) shows the energy difference between the occupied edge state and the dispersive states closest to the Fermi level, which is denoted as dE. Spin polarization is realized if dE $>$ 0. The same argument holds in the case of doping an electron (n-type doping). Since the energy difference between the unoccupied dispersive states and unoccupied edge states is smaller than that between the occupied dispersive states and occupied edge states, p-type substitutional doping of the (9,0) z-$C_2(BN)_2$ easily gives rise to spin polarization while n-type doping does not. However, the unoccupied dispersive states are sufficiently higher than the unoccupied edge states in some cases, meaning that n-type doping still leads to the magnetic ground state. Indeed, in the case of (10,0) nanotubes, where the difference in energy between the occupied and unoccupied edge states is larger than that of (9,0) nanotubes, n-type doping also leads to the spin polarized electronic structure. Therefore, any type of atom substitution can induce magnetism in larger-diameter nanotubes. Hereafter, I focus on the p-type substitutional doping, in which one N atom is replaced with one C atom at a C-N bond. The other p-type doping, where one C atom is replaced with one B atom at a C-N bond, has no effect on my conclusion.

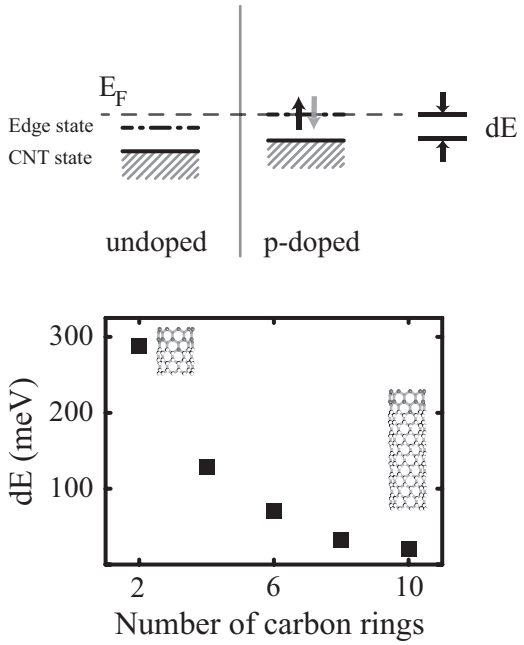

FIGURE 4.11: (a) Relative energy of edge and dispersive state closest to the Fermi level of undoped and p-doped nanotube. (b) Energy difference between the edge and dispersive states as function of length of CNT.

4.3.3 Transport through edge states

Let us discuss the spin transmission through a zigzag CNT/BNNT heterojunction. Since the primary importance is attached to the magnetic moment of the carbon/boron-nitride nanotube, the occupation of the zigzag CNT edge states is crucial for the spin polarization. When a short BNNT is simply connected to semi-infinite CNT electrodes, the injected holes by the substitution will be filled with electrons from the nearby C atoms in the electrodes. Hence, the model, in which a short inner CNT is connected at both its ends to the BNNTs and all of these components intervene between the outer CNTs, is employed as shown in Fig. 4.7. Here and hereafter, I refer to this transport model as CBNNT. To make sure that the positions of the edge states and the dispersive states of the inner CNT are less sensitive to the length of the outer CNTs with respect to the Fermi level, I first examine the electronic band structure upon increasing the length of the outer CNT. Figure 4.12 shows the computational models and band structures of the CBNNTs without the doped atom. The energies of the edge states and the dispersive states of the inner CNT for all models are insensitive to the length of the outer CNT and the edge states always lie above the dispersive states. Electron will be removed from the edge states in the inner CNT upon the substitutional doping regardless of the length of the outer CNT. Therefore, we can conclude that the mechanism of the spin polarization in the CBNNT is the same as that of the z-$C_2(BN)_2$ in the previous section.

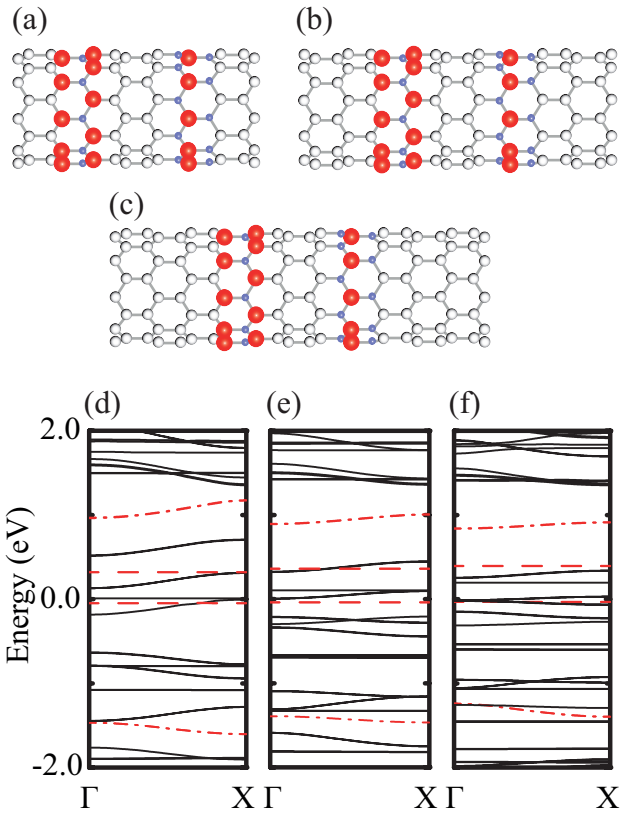

FIGURE 4.12: (a)-(c) Computational models of CBNNTs without doped atom upon increasing length of outer CNT. (d), (e), and (f) Band structures of models (a), (b), and (c), respectively. The solid, dashed, and dashed-dotted curves indicate the states of the outer CNT, the edge states, and the dispersive states of the inner CNT, respectively. Zero energy was chosen as the Fermi level. Meaning of symbols are the same with those in Fig. 4.7.

Figure 4.13(a) shows the conductance spectra of the CBNNT for electrons coming from the left electrode. Except for the peaks $B_\uparrow$ and $C_\uparrow$, there is a one-to-one correspondence between the peaks in the spin-up and spin-down conductance spectra. I also plot in Fig. 4.13(b) the charge density of the scattering waves integrated on the x-y plane indicated by the arrow in Fig. 4.7. It is found that the spin-down charge density is almost zero while four peaks a, b, c, and d corresponding to the peaks $A_\uparrow$, $B_\uparrow$, $C_\uparrow$, and $D_\uparrow$ in the conductance spectrum are observed in the spin-up charge density.

To investigate the origin of significant peaks of the conductance spectra in more detail, I depict in Fig. 4.14 the isosurfaces of the charge density distribution of the scattering waves for electrons injected from the left electrode. One can see that the distributions corresponding to the peaks $B_\uparrow$ and $C_\uparrow$ are localized at the zigzag edge whereas those corresponding to the peaks $A_\uparrow$, $A_\downarrow$, $D_\uparrow$, $D_\downarrow$, $E_\uparrow$, and $E_\downarrow$ are extended in the outer CNT region. Figure 4.15 shows the charge density distribution of the two spin-up edge states of the periodic model, which are denoted by α and β in Fig. 4.8(g). The distribution of the energetically lower spin-up edge state α is localized along one half of zigzag CNT

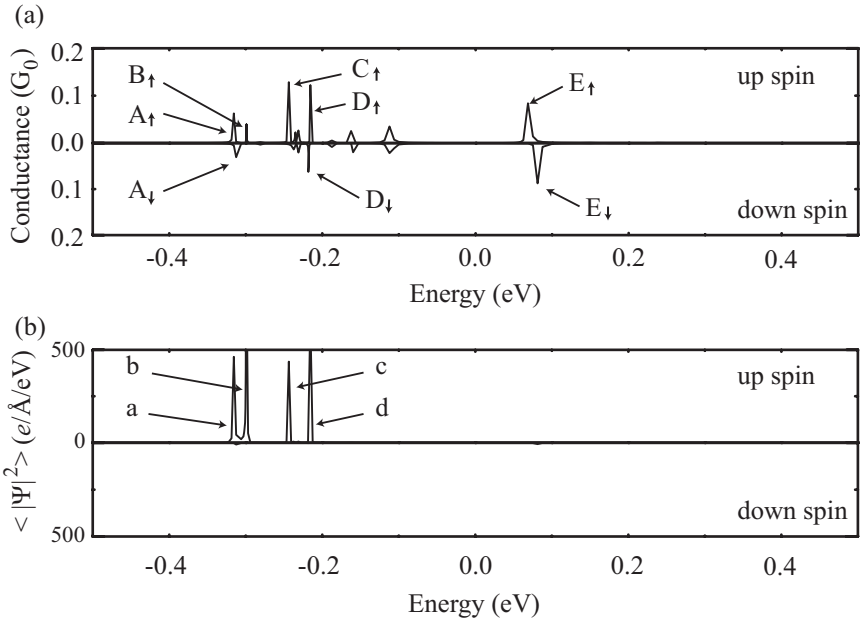

FIGURE 4.13: (a) Conductance spectra of CBNNT as functions of energy of incident electrons. (b) Charge density of scattering waves for electrons coming from left electrode integrated on the plane indicated by the arrow in Fig. 4.7. Zero energy was chosen as the Fermi level.

edge and that of the higher spin-up edge state β is aligned along the other half of the zigzag CNT edge. Thus, it is concluded that the peak $B_\uparrow$ ($C_\uparrow$) originates from resonant tunneling by the lower (higher) spin-up edge state α (β) and the peak $A_\uparrow$ ($D_\uparrow$) is the contribution owing to the hybridization of the outer CNT and the lower (higher) spin-down edge states. In addition, the peaks $E_\uparrow$ and $E_\downarrow$ as well as the other small peaks in the conductance spectra are related to the states in the outer CNT.

In the case of the undoped BNNT, there are no contributions of the edge states to the electron transport [4]. I have also assured that the conductance of the present model without the doped atom between the energy range of -0.8 eV and 0.6 eV, in which the edge states lie in Fig. 4.8(b), is less than $10^{-3}G_0$. On the other hand, the edge states conduct electrons as a result of the distortion of the symmetry and the transport property is the spin-dependent in the doped C/BN nanotube. Thus, the substitutional doping plays important roles for the transport through the edge states as well as the spin-polarized electronic structure.

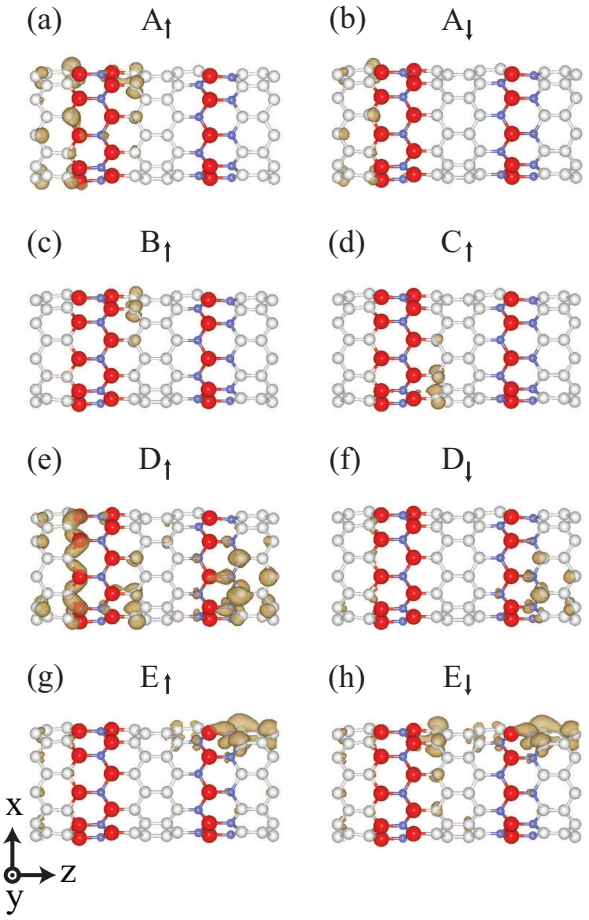

FIGURE 4.14: Isosurfaces of charge density distributions of scattering waves emitted from left electrode of CBNNT at energy of peaks (a) $A_{\uparrow}$, (b) $A_{\downarrow}$, (c) $B_{\uparrow}$, (d) $C_{\uparrow}$, (e) $D_{\uparrow}$, (f) $D_{\downarrow}$, (g) $E_{\uparrow}$, and (h) $E_{\downarrow}$ in Fig. 4.13(a). The isovalue is 5×10^{-2} $e/\text{Å}^3$/eV in (a), (b), (c), (d), (e), and (f), and the isovalue is 5×10^{-4} $e/\text{Å}^3$/eV in (g) and (f). Meaning of symbols are the same with those in Fig. 4.7.

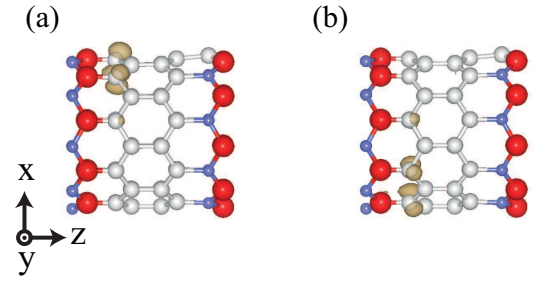

FIGURE 4.15: Isosurfaces of charge density distributions of (a) energetically lower spin-up edge state indicated by α in Fig. 4.8(g) and (b) energetically higher spin-up edge state indicated by β. The isovalue is 7.5×10^{-4} $e/\text{Å}^3$. Meaning of symbols are the same with those in Fig. 4.7.

4.4 Summary

I have examined the electronic structures and electron-transport properties of (9,0) carbon/boron-nitride nanotubes in which CNTs are sandwiched between BNNTs by first-principles calculations using DFT. It is found that p-type and n-type substitutional dopings are not equivalent in the case of smaller-diameter nanotubes because the σ-π hybridization owing to the small curvature pulls down the energetically dispersive states, which results in the nonmagnetic ground-state electronic structure for n-type doping. On the other hand, the spin polarization can be observed by n-type doping when the diameter of nanotubes increases. Moreover, unlike the nanotubes without doped atoms, where the edge states do not contribute to the electron transport because of the symmetry mismatch with the conducting states of CNT, the alternation of the symmetry of the edge states owing to the presence of the doped atom gives rise to the spin-dependent resonant tunneling through the edge states. The calculation reveals that the doped atom affects the transport property as well as the spin-polarized electronic structure of the heterojunction and indicates that the distortion of the symmetry is important for the electron transport through the edge states. Although it is not easy to fabricate such CBNNT structure using present experiment techniques, I hope that future experiment techniques can be used to fabricate the CBNNT structures because similar structures have been realized by bottom-up or top-down methods. In addition, it is well known that SOC in first-row elements is tiny. To overcome the small MAE of the first-row elements, I suggest that the magnetic moment of the structures can be fixed by doping heavy elements such as As or Ga, decorating the CBNNT on a magnetic surface, or bundling tubes. I would like to investigate such systems in a future study.

Chapter 5

Electronic Structures of Carbon-Incorporated Gold Nanowires

5.1 Introduction

A single metal atom nanowire is an ultimate one-dimensional material. Its physical and chemical properties are of great interest from the point of view of fundamental science. One of their observed remarkable properties is quantized conductance, clearly seen even at room temperature [66–68]. A gold atom nanowire has been confirmed to have a quantized unit of conductance ($1G_0 = 2e^2/h$, where e is the electron charge and h is Planck's constant), using transmission electron microscopy (TEM) combined with scanning tunneling microscopy (STM) [69] and the mechanical controllable breaking junction (MCBJ) method [70]. Other than gold, noble and alkali metal nanowires have been reported to show quantized conductance [67, 71, 72]. In addition, the strong bond strength of a metal atom nanowire has been pointed out as being very significant [73, 74]. The breaking force of a gold atom nanowire was measured to be 1.5 nN, higher than expected for individual bonds in bulk gold (0.8–0.9 nN) [74].

A nanowire of atoms has been typically synthesized to date by pulling a thin metal neck suspended between two electrodes. During pulling, the metal neck is discontinuously thinned due to plastic deformation until it breaks. A pure gold atom nanowire has been observed to be a maximum of two or three atoms in length [69, 75]. Recent theoretical studies, however, suggest that the Au-Au-O-Au-Au structure is so strong that more gold atoms can be extracted from the electrode upon pulling [76, 77]. Other than an oxygen atom, hydrogen and carbon atoms have also been suggested for incorporation to

form long gold atom nanowires [78–82]. Experimentally, long gold atom nanowires were reported to be formed by extracting gold atoms one by one from an electrode surface [83]. Either oxygen atoms or hydrogen molecules were thought to be incorporated in the observed nanowire, but this could not be unambiguously clarified. It is difficult to detect such light element impurity atoms incorporated in the nanowires.

Using ultrahigh vacuum (UHV) TEM combined with STM [84], Oshima *et al.* discovered that long gold atom nanowires could be reproducibly synthesized from a carbon-contaminated gold surface at room temperature [5], as shown in Figs. 5.1 and . 5.2. Since the UHV condition minimized the presence of residual gases such as oxygen, nitrogen, and hydrogen in the microscope, the observed long gold nanowire was judged to be formed by the incorporation of carbon atoms.

In their TEM images, somewhat amorphous contrast was sometimes observed at the surface of one or both electrodes even after strong electron-beam irradiation. This was judged to correspond to a carbon-contaminated surface, since a very narrow gold contact formed by the connection of such electrodes did not show clear quantized conductance, as in a pure gold contact. They found that a long gold atom nanowire was formed between two electrodes only when the amount of carbon atoms on the surfaces of the two electrodes was so small that carbon atoms did not clump to form agglomerates. When the amount of carbon atoms was large on one electrode surface, carbon atoms migrated and clumped to form agglomerates by contacting the two electrodes and applying a bias voltage. Furthermore, the agglomerates changed into graphitized structures, such as graphene, nanotubes, and fullerenes, when the bias voltage increased above 0.5 V, and the fullerene was formed by such a process.

In most of their experiments, the amount of carbon atoms on the electron surface was rather large in the initial stages. As previously mentioned, fullerene was naturally formed between two electrodes when contacting the two electrodes under a bias voltage. However, a small amount of carbon atoms sometimes remained on one or both electrodes after the formation of the fullerene. They found that a long gold nanowire was synthesized between such a carbon-contaminated surface and the carbon fullerene. The fullerene did not play a role in the synthesis of the long gold atom nanowire, since they also observed that a long gold atom nanowire was synthesized even in the absence of the fullerene.

In the TEM images in Fig. 5.1, the dark dots were gold atoms and the number of gold atoms in the nanowire increased one by one from three to seven [Figs. 5.1(a)– 5.1(e)]. Such a long nanowire has not been observed previously for pure gold atoms. The atom interval was estimated to be 5.0 Å. Conductance evolution measured simultaneously with the pulling process, showed a spiky peak at the same time the nanowire was relaxed by

introducing a single gold atom. In the previous report, it has been suggested that interatomic distances as large as 5.0 Å cannot be explained without the presence of carbon atoms [85].

In the images shown in Fig. 5.2, the positions of the individual gold atoms were recognized with atomic spacing of 5.0 Å. They found that this nanowire was so strong that it remained intact even when it was bent during pulling. Although a pure gold atom nanowire has not been allowed to be bent when stretching [69], a gold atom nanowire with incorporation of impurity atoms has been reported to be bent in the TEM observation [83]. Furthermore, in the pulling process, the surface layer (indicated by the arrowhead in Fig. 5.2) is gradually removed from the bottom electrode. The point of contact of the long nanowire with the electrode surface moves towards the left side. Finally, the surface layer is completely removed from the electrode. Therefore, they supposed that the (111) surface is reconstructed by the adsorbed carbon atoms to form a one-dimensional configuration consisting of gold and carbon atoms, and the long nanowire is obtained by pulling such a one-dimensional configuration. Based on their experiments, in this chapter, I focus my study on the electronic structures and the formation of carbon-incorporated gold nanowires on gold (111) surface by first-principles calculations.

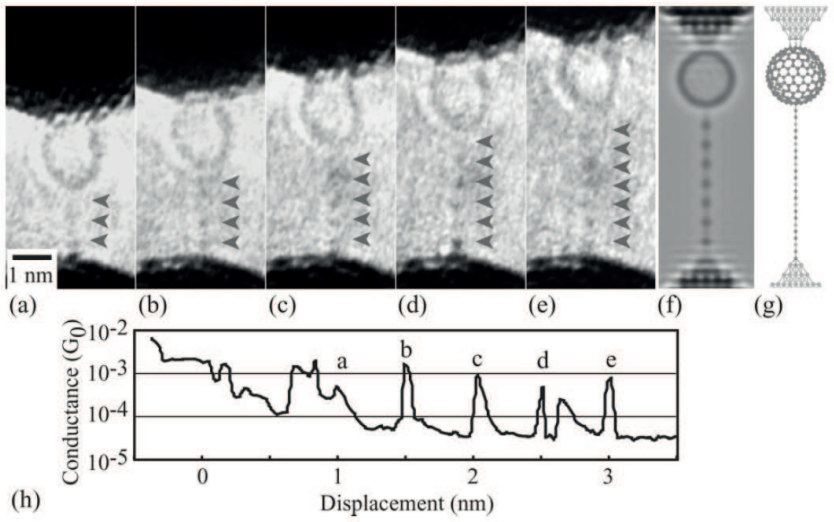

FIGURE 5.1: (a)–(e) A series of TEM images taken at each introduction of a gold atom to a gold atom nanowire during pulling from the bottom electrode. The number of gold atoms, indicated by arrows, increased from three to seven. The distance between two gold atoms is 5.0 Å. (f) Simulated TEM image of a nanowire consisting of seven gold atoms. The image contrast of each gold atom in the nanowire is similar to that in the fullerene structure. Carbon atoms in the nanowire are not visualized. (g) A model of the nanowire including both electrodes; the fullerene is attached to the upper electrode. The nanowire has two carbon atoms at each gold atom interval (5.0 Å). The fullerene is assumed to be a spherical C_{240}. (h) Evolution of conductance as a function of displacement during pulling of the nanowire. A spiky peak appears for each 5.0-Å displacement. Figure is taken from Ref. [5].

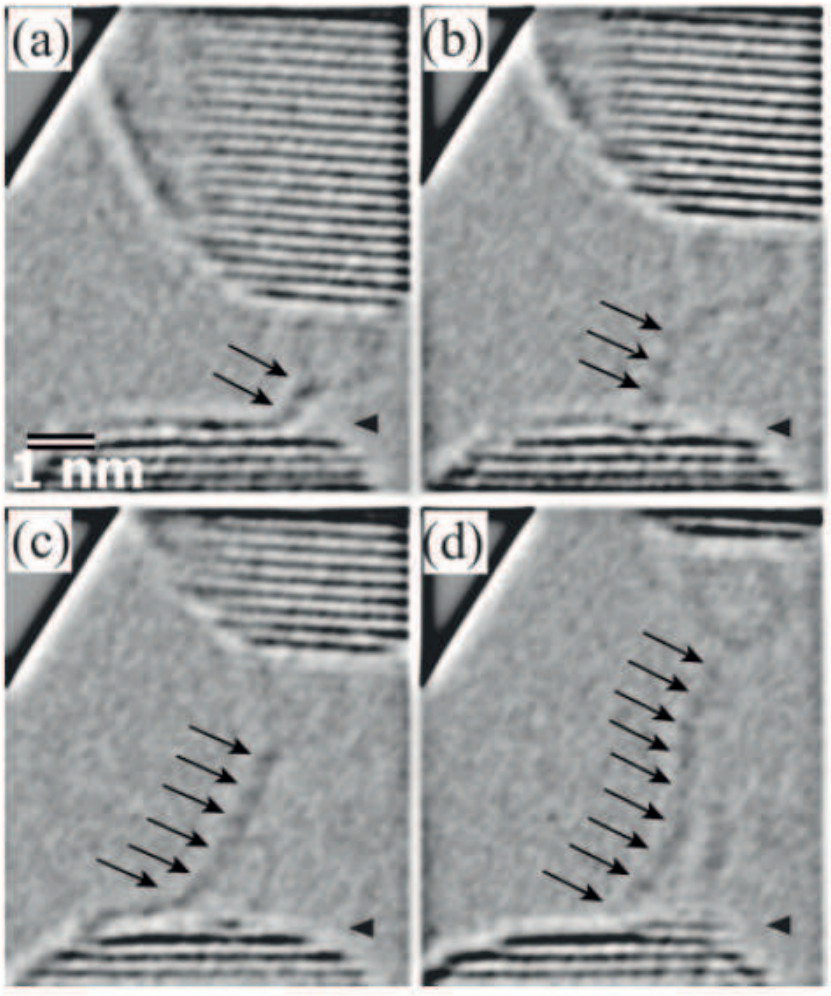

FIGURE 5.2: Another series of TEM images during pulling of the nanowire from the gold surface. Since the nanowire continuously fluctuated during stretching, individual gold atoms were hardly recognized in the raw image. The image contrast was thus enhanced by using a band-pass filter. Both electrodes have a gold (111) surface. The surface layer of the bottom electrode shows different contrast from those of the lower layers. Also, the spacing between the surface and second layer is slightly wider than the gold (111) lattice spacing. (a)–(c) The surface layer is gradually removed from the bottom electrode. The nanowire grows smoothly, even though it bends to a large extent. (d) The surface layer is completely removed from the electrode. In (c) and (d), an extra nanowire is seen synthesized at the right side of the long nanowire. Its intensity was similar to the gold atoms in the long nanowire. Figure is taken from Ref. [5].

5.2 Computational models

As discussed in the introduction, experimental results suggest that the gold nanowires may already be formed on the gold (111) surface. I performed the calculations for both freestanding gold nanowires and gold nanowires on the gold (111) surface. Theoretical calculations were carried out within the framework of DFT [9] using the real-space method [16]. Projector augmented-wave method [31, 32] was employed to describe the interactions between ions and electrons and the exchange-correlation interaction was treated by local density approximation [9].

Figure 5.3 shows the computational models of freestanding gold nanowires with carbon incorporation. The computational model of gold nanowires on gold (111) surface is shown in Fig. 5.4. Three layers of gold were used to simulate the gold (111) surface. The supercell was chosen to be 5.76 Å (along the $\langle 110 \rangle$ direction) $\times$ 5.00 Å (along the $\langle 112 \rangle$ direction) under periodic boundary conditions, where 2.88 Å is the interatomic distance in bulk gold. Each layer contains 4 gold atoms and the interlayer distance is 2.36 Å. A vacuum region of 10 Å was inserted in the (111) direction perpendicular to the surface to avoid spurious interactions between periodic supercells. A grid of 2×2 **k**-point sampling was employed and a grid spacing of 0.185 Å was used. Structural optimization was performed until the remaining forces were less than 0.05 eV/Å.

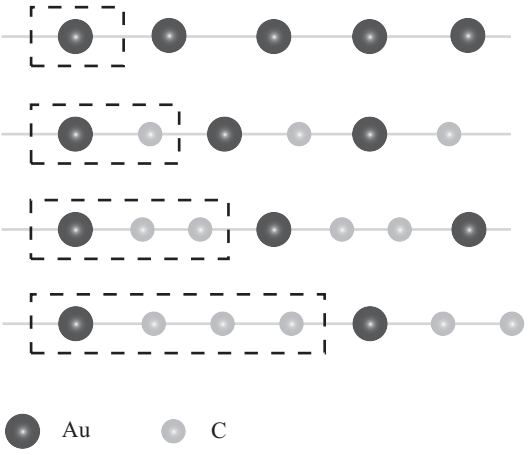

FIGURE 5.3: Computational models of freestanding gold nanowires and gold nanowires with 1, 2, and 3 carbon atoms incorporation. The dashed rectangulars represent the supercells.

When the gold nanowire were put on the (111) gold surface, the gold atomic distance is not the same with that of the freestanding gold nanowire because gold atom prefers being situated at a triangular lattice site which has the lowest energy. In the Au-C structure, I assumed that gold atoms are aligned along the $\langle 1\bar{3}2 \rangle$ direction at a 3.3 Å interval and a single carbon atom was inserted at each 3.3 Å interval. In this structure, every two gold atoms along the structure are not at triangular lattice sites. In the Au-C_2

structure, I assumed that gold atoms are along the ⟨112⟩ direction with a 5.0 Å interval and two carbon atoms are inserted at each 5.0 Å interval. In the Au-C_3 structure, I assumed the gold atoms to be along the ⟨110⟩ direction at a 5.8 Å interval and three carbon atoms are inserted at each 5.8 Å interval.

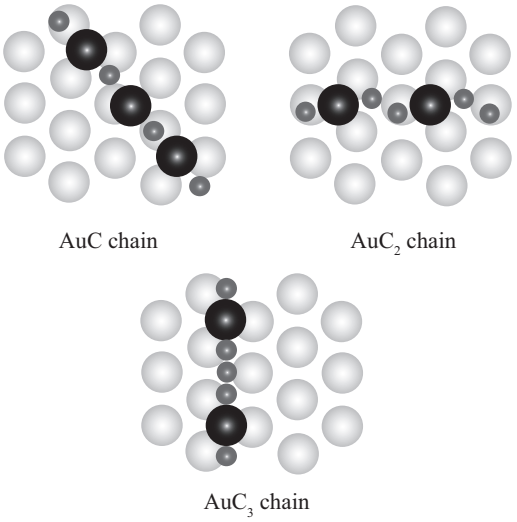

FIGURE 5.4: Computational models of gold nanowires with 1, 2, and 3 carbon atoms incorporation on gold (111) surface. White, black, and grey spheres denote substrate gold atoms, gold atoms on the surface, and carbon atoms, respectively.

5.3 Results and discussion

In the case of freestanding gold nanowire, the gold interatomic distance is 2.7 Å. The gold nanowire will break if the gold interatomic distance reaches 3.0 Å, implying that the long gold interatomic distance observed by experiments [86] was due to the incorporation of light elements into gold nanowire. Light elements such as carbon are inserted between neighboring gold atoms, stabilizing and enlarging the nanowire. When the number of carbon atoms incorporated between gold atoms was one, two, and three (named Au-C, Au-C_2, and Au-C_3, respectively), the calculated distances between two neighboring gold atoms were 4.0, 5.0, and 6.4 Å, respectively. These values are close to those reported by previously theoretical and experimental studies [78, 86, 87]. Among these values, the long atomic gold nanowire was determined to be the Au-C_2 structure. Figure 5.5(a) shows force curves of freestanding gold nanowires. The breaking force is 3.6 eV/Å for the Au-C_2 structure, which is much higher than that of 1.3 eV/Å for a pure gold nanowire.

The experimental results suggested that a one-dimensional configuration consisting of gold and carbon atoms was formed on the surface layer of the gold electrode when the amount of carbon atoms on the surface was small. Carbon atoms are likely to be inserted at the interval between two lattice points of the triangular network at the gold (111) surface. I assume that one-dimensional configurations were formed on the gold (111) surface, corresponding to Au-C, Au-C_2, and Au-C_3 structures, and the calculated formation energies are shown in Fig. 5.5(b). For a gold nanowire on a gold (111) surface, the gold interatomic distance is not the same as that of the freestanding gold nanowire since the gold atoms favor to be located at the lattice points of a triangular network on the gold (111) surface, which lowers the formation energy. The formation energy of each structure was obtained by the formula

$$\Delta E = E_{AuC_n} - E_{surf} - E_{Au} - n \times E_C, \tag{5.1}$$

where,

E_{AuC_n} is the total energy of the system with the gold nanowires adsorbed on the gold (111) surface,

E_{surf} is the total energy of the bare gold (111) surface,

E_{Au} is the total energy of a gold adatom on the gold surface, defined as the energy difference between the total energy of the bare gold surface and that of the gold surface with an gold adatom,

E_C is the total energy of a carbon atom adsorbed on the gold surface, which depends on the initial binding state of the carbon atom,

and n is the number of carbon atoms in the supercell.

The formation energy is a function of the chemical potential of carbon atom per supercell, E_C, which depends on the average coordination number per carbon atom.

The formation energy is a function of the total energy of carbon atom adsorbed on the gold surface, E_C, which is –241.6 eV for graphene (described by $E_C^{(1)}$), –239.9 eV for a pair of carbon atoms ($E_C^{(2)}$), in which one carbon atom is adsorbed at the fcc hollow site and the other is adsorbed at the neighboring hcp hollow site, and –239.2 eV for a single carbon atom ($E_C^{(3)}$) adsorbed on the fcc hollow site. The quantity, $E_C^{(1)}$, corresponds to the case of graphene that serves as the lower bound of E_C, while $E_C^{(3)}$ serves as the upper bound of E_C.

The formation energy in Fig. 5.5(b) gradually decreases with increasing the total energy of carbon atom adsorbed on the gold surface, E_C (corresponding to decreasing average coordination number per carbon atom). The Au-C_2 structure is the most favorable one-dimensional configuration formed on the gold (111) surface when the number of carbon atoms adsorbed at the gold (111) surface is small. On the other hand, when the number of carbon atoms adsorbed on the gold (111) surface is larger than a certain value, the formation of a graphene-like sheet is more favorable than any of the one-dimensional configurations. These calculated results reproduce well the experimental observations. Hence, it is possible to conclude that the observed long nanowire has two carbon atoms at each interval between two gold atoms, formed at the carbon-contaminated gold (111) surface before pulling.

5.4 Summary

I have investigated the electronic structures of carbon-incorporated gold nanowires by first-principles calculations using DFT. It is found that carbon dimer is incorporated between neighboring gold atoms of gree-standing gold nanowires leading to the long gold atomic spacing observed in the experiment. The calculated formation energies show that the nanowire has two carbon atoms at each gold atom interval of 5.0 Å and is constructed along the $\langle 112 \rangle$ direction on the carbon-adsorbed gold (111) surface as a stable one-dimensional configuration before pulling. The present study shows that the carbon atoms act as glue for forming the long gold nanowire, which is a unique behavior in one-dimensional structures.

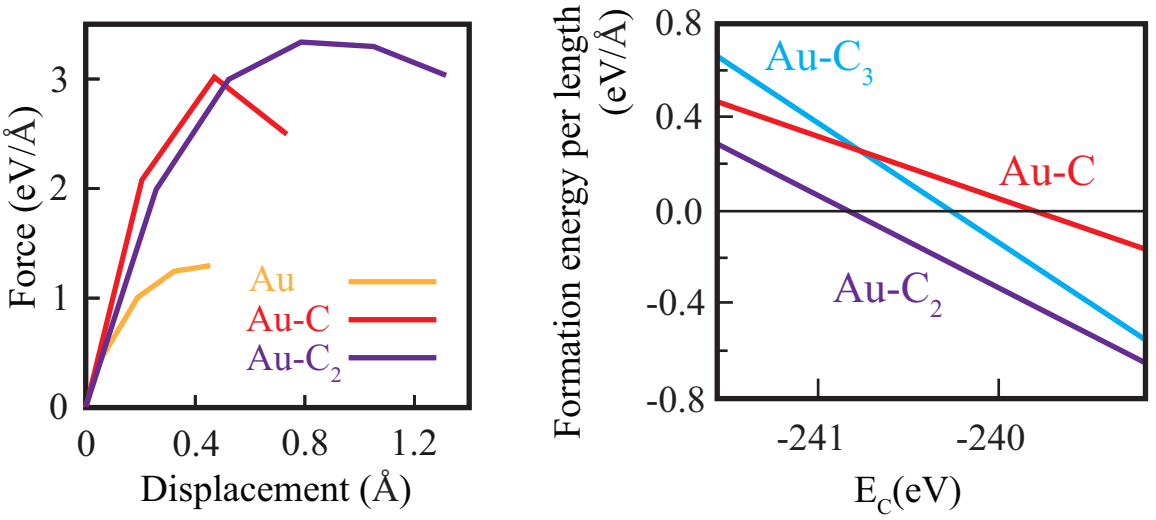

FIGURE 5.5: (a) Force curves of a pure gold atom nanowire as well as the nanowires having one and two carbon atoms at each gold atom interval, named Au-C and Au-C_2, respectively, as a function of displacement. (b) Formation energy per length of Au-C, Au-C_2, and Au-C_3, the structure of each of which is schematically illustrated in the insert, as a function of the total energy of carbon atom adsorbed on gold surface, E_C. Figure is taken from Ref. [5].

Chapter 6

Electronic Structures and Electron-Transport Properties of Thiol-Terminated Porphyrin Wires

6.1 Introduction

Controlling electron transport through molecules that bridge two electrodes is a basic step toward the development of sophisticated nanoscale devices [88, 89]. For such molecular conductors, there has been a great interest in understanding the impact of π-conjugation, magnitude of optical and potentiometric band gaps, molecular length, electrode material, and mode of molecule-to-electrode connectivity on molecular electrical conductance and transport mechanisms [90–92].

A variety of techniques has been developed to form metal-molecule-metal junctions and evaluate electrical functionality such as conducting atomic force microscopy, crossed-wire tunnel junctions, as well as mechanically controlled and scanning probe microscopy (SPM) break junctions, i.e., scanning tunneling microscopy (STM) and conducting probe atomic force microscopy break junctions [89, 93–95]. These methods have been employed to study the conductances of widely varying molecular structures [93–95], with SPM-based break junction techniques showing particular efficacy to interrogate conjugated structures having substantial length ($>$ 20 Å), including oligophenyleneimines, butadiyne-bridged multi(porphyrin) systems, oligothiophenes, poly(*p*-phenyleneethynylene)s, and oligo(pentaphenylene)s.

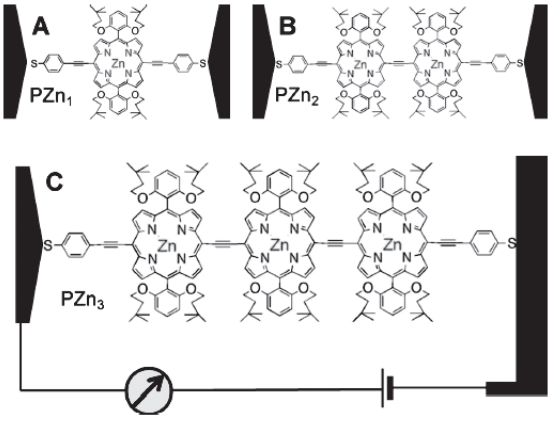

FIGURE 6.1: Zinc porphyrin molecules suspended between gold STM tip and gold substrate. Figure is taken from Ref. [6]

In the classes of conjugated structures in which single molecule charge transport measurements have been performed, meso-to-meso ethyne-bridged (porphinato) zinc(II) structures (see Fig. 6.1) show exceptional electronic structural characteristics. The traditional uses of porphyrin molecules have been as dyes due to their intense absorptions in the visible light. Recently, there has been renewed interest in these molecules as their electronic and photoelectrochemical properties can be exploited for applications including multibit storage [96, 97], memory elements [39], and photovoltaics [98]. By STM break junction method Li *et al.* fabricated nanowires formed by thiol-terminated porphyrin molecules suspended between a gold STM tip and a gold (111) substrate [6]. They found a stepwise feature of the conductance during the pulling process of the STM tip as seen in Fig. 6.2. The low-conductance state was observed after the high-conductance one as the molecular junction was elongated. The origin of this dual conductance responses is unknown and could be thought to derive from variations in the molecule-electrode contact geometry or in molecular conformation.

During the stretching of the STM tip, sulphur atoms at two ends of the porphyrin wires can have different bonding geometries with the gold substrate, giving rise to different conductance states. Experimentally, it has been found that the force required to break a molecular junction of a single octanedithiol molecule attached to gold electrodes is similar to the value of the force required to break a gold-gold bond in an atomic gold chain [74]. This fact strongly suggests that the dithiol molecule can pull gold atoms off the electrodes when an external force is applied. Molecular dynamics simulations also indicate that a thiolate molecule can pull gold atoms off a stepped surface [99]. Previous DFT studies on bezenedithiols and alkanedithiols molecular junctions pointed out that the conductances of the junctions, in which sulphur atom is attached to a gold adatom on gold (111) surface, decrease by two-order of magnitude compared to those of the junctions, in which sulphur atom bonds to a hollow site of the gold surface [100–102].

However, no theoretical studies have been made to investigate the dual conductance responses in the thiol-terminated porphyrin wires, although these systems can be utilized in molecular-based switches [103]. In this chapter, I investigated the electronic structures and electron-transport properties of thiol-terminated porphyrin wires by first-principles calculations.

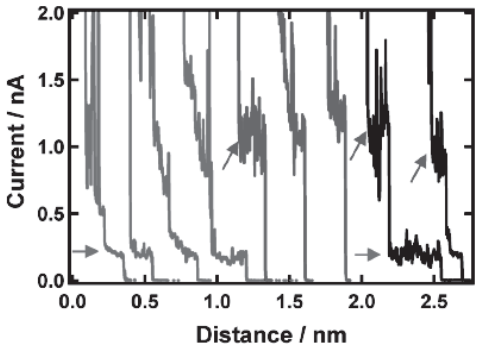

FIGURE 6.2: Current-distance traces recorded during STM break junction experiment for single zinc porphyrin molecular junction at $V_{bias} = 0.1$ V showing high- and low-conductance traces. Figure is taken and revised from Ref. [6].

6.2 Computational models

The first-principles calculations are performed within the framework of DFT using the real-space finite-difference approach [15], which enables us to determine the self-consistent electronic ground state with a high degree of accuracy using a time-saving double-grid technique [16, 28–30]. The electron-ion interaction is described using projector augmented-wave method [31, 32], and the exchange-correlation interaction is treated within the local density approximation [9].

Figure 6.3 shows the computational models employed to study the transport properties through porphyrin molecules, in which the periodicity is imposed in the x- and y-directions. Two transport models are investigated, in which the sulphur atom of the porphyrin molecule bonds to hollow site or a gold adatom of gold (111) electrode, and shall be referred as hh and aa structure, respectively. The gold adatom is used in the aa structure since gold atoms can migrate to positions between the electrode surface and thiol terminations as the electrodes are pulled apart. My models qualitatively capture the changes in the contact geometry as has been discussed for the benzenedithiol and alkanedithiol molecular junctions [101, 102, 104, 105]. Although the phenyl and porphyrin rings can have relative angle to each other, I study here the planar configuration as a representative since it has been reported that the torsion of some conjugated molecules can be manipulated by laser pulses [106–108]. The electron transport property is computed using scattering wave functions continuing from one electrode to the other, which

are obtained by the overbridging boundary-matching method [16, 57]. The Kohn-Sham effective potential in the scattering region is first calculated under the periodic boundary conditions, and then the wave functions are obtained non-self-consistently. The size of scattering region corresponding to the hh structure is $L_x = 19.95$ Å, $L_y = 11.52$ Å, and $L_z = 35.40$ Å, and that of scattering region corresponding to the aa structure is $L_x = 19.95$ Å, $L_y = 11.52$ Å, and $L_z = 40.12$ Å, where L_x, L_y, and L_z are the lengths in the x-, y-, and z-directions, respectively. A grid spacing of 0.2 Å is employed and the Brillouin zones of the scattering regions are sampled by 4 k-points along the z-axis to set up the Kohn-Sham effective potential. The Au-S distance is initially chosen as 2.35 Å, according to Ref. [104, 109–112]. The Au-Au interatomic distance is 2.88 Å, and the gold interlayer distance is 2.36 Å, according to Ref. [5]. All the atoms in the scattering region except the second gold atomic layers are relaxed until the remaining forces are less that 0.05 eV/Å. The conductance under zero temperature and zero bias is described by the Landauer-Büttiker formula [59], $G = G_0 \sum_{i,j} |t_{ij}|^2 \frac{v_i}{v_j}$, where t_{ij} is the transmission coefficient at which electrons are transmitted from an initial mode j to a final mode i inside the scattering region, v_i and v_j are the longitudinal components of the group velocity in modes i and j, $G_0 = e^2/h$, with e and h being the electron charge and Planck's constant, respectively.

6.3 Results and discussion

Figures 6.4(a) and 6.4(b) show the local density of states (LDOS) of the hh and aa structures, respectively. The LDOS is plotted by integrating them along the x-y plane, $\rho(z, E) = \int |\psi(\mathbf{r}, E)|^2 d\mathbf{r}_{||}$, where $\mathbf{r} = (x, y, z)$, ψ is the wave function, and E is the energy of the states. Near the Fermi level, the majority of charge density in the hh structure is confined at the center of porphyrin molecule, whereas that in the aa structure is localized at the contact between porphyrin molecule and gold electrode. From charge density distribution, I found that the coupling between d_{xz} orbitals of gold adatom and p_z orbitals of sulphur atom induces large density of states just below the Fermi level in the aa structure. Thus, different transport modes are expected for the hh and aa structure in the vicinity of the Fermi level. At 0 eV, the conductance of the hh and aa structure are 1.31×10^{-2} and 3.49×10^{-1} G_0, respectively. Because sulphur has larger electronegativity than gold, more electrons are transferred to the porphyrin ring in the aa model. As a result, the electronic states of the molecule are shifted towards the Fermi level, leading to the increase in the conductance.

The conductance of the hh structure is reduced by one-order of magnitude compared to that of the aa structure, suggesting that the hh and aa structures correspond to the low-

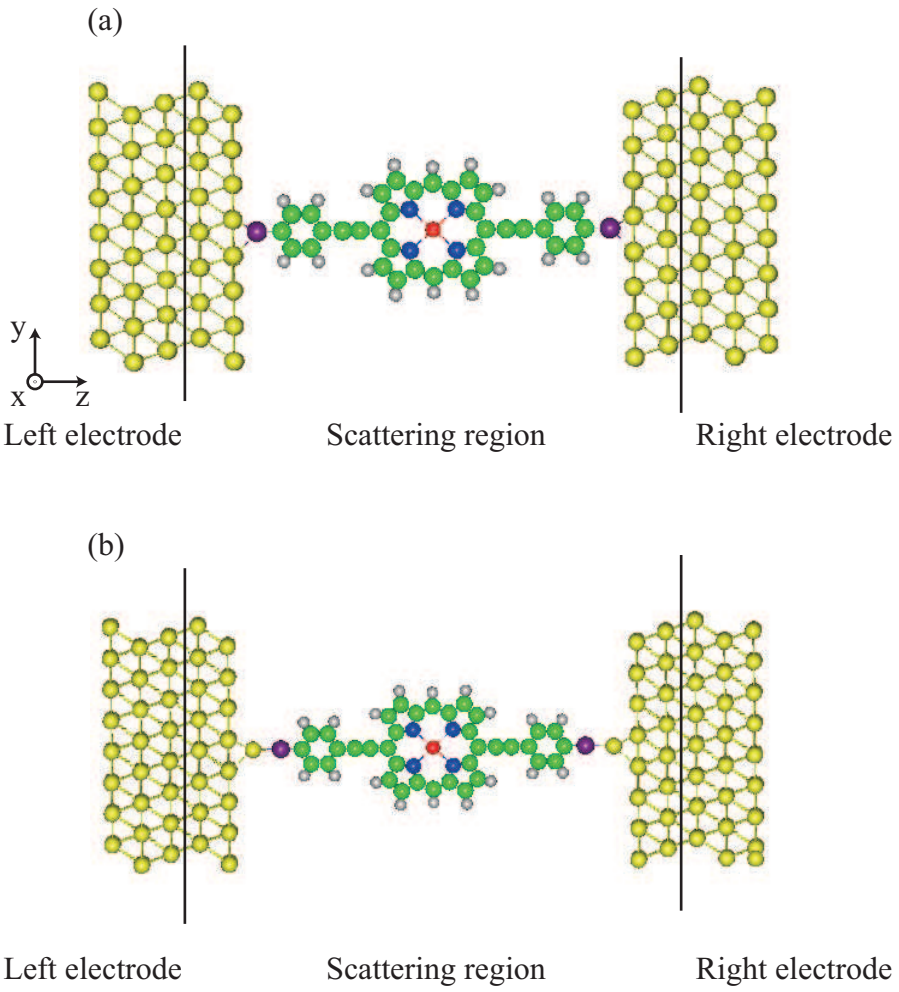

FIGURE 6.3: Computational model of (a) aa and (b) hh structure suspended between gold (111) electrodes. The white, green, blue, red, purple, and yellow spheres indicate hydrogen, carbon, nitrogen, zinc, sulphur, and gold atoms, respectively.

and high-conductance states. The results indicate that the high-conductance state of the porphyrin wires are due to changes in the contact geometry in which sulphur atom bonds to a gold adatom of the gold substrate.

6.4 Summary

I have studied the electronic structures and electron-transport properties of thiol-terminated porphyrin wire using first-principles calculations within the framework of DFT. The results show that different interface states are found for the aa and hh structures, in which sulphur atoms of porphyrin molecule are attached to gold adatoms and hollow sites of gold (111) surface. Near the Fermi level, the majority of charge density is located at the center of porphyrin molecule in the hh structure, and at the molecule-electrode interface in the aa structure. At 0 eV, the conductance of the hh structure

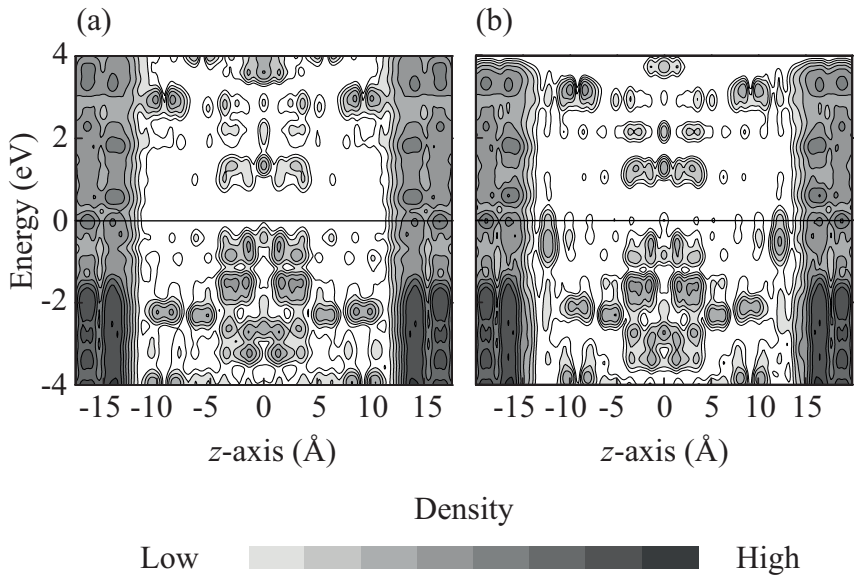

FIGURE 6.4: Distributions of LDOS of (a) hh and (b) aa structure integrated on plane parallel to interface as functions of relative energy from Fermi level. Zero energy is chosen to be at the Fermi level. Each contour represents twice or half the density of the adjacent contour lines, and the lowest contour is 6.78×10^{-5} e/eV/Å.

is one-order of magnitude smaller than that of the aa structure. In the aa structure, electrons are transferred from the gold atoms to the molecule, resulting in the energy shift of the molecule states towards the Fermi level and an increase in the conductance.

Concluding Remarks

Major findings

In this thesis, I have used first-principles calculations based on density functional theory to study:

- The electronic structures and magnetic anisotropy energies of graphene with an absorbed Fe, Co, or Ni adatom. I found that spin polarizations are observed in the case of the Fe and Co adsorption. In the case of Ni adsorption, the Rashba effect is realized with a **k**-dependent energy shift at the bottom of the Fermi surface of π bands. The calculated magnetic anisotropy energies indicate an in-plane easy axis for the Fe adatom, in contradiction with experiment, and an out-of-plane easy axis for the Co adatom, in agreement with experimental observation. The occupation of E_1 orbitals, comprising of d_{xz} and d_{yz} orbitals, is important to determine the direction of the easy axis of the Fe and Co adatoms.

- The electronic structures and electron-transport property of carbon/boron-nitride nanotubes. The calculations show that localized edge states are observed at zigzag boundary between carbon and boron-nitride nanotubes. The occupation of the edge states gives rise to the spin polarization in the case of p-type substitutional doping at the zigzag carbon nanotube edge. The σ-π hybridization due to the curvature pulls down the energetically dispersive states, resulting in the nonmagnetic ground-state electronic structure in the case of n-type doping. Although it has been reported that the electron transport through the edge states in the undoped nanotube is prevented by the rotational symmetry mismatch between the edge and carbon nanotube states, I found that the alternation of the symmetry due to doped atom leads to the spin-dependent resonant tunneling through the edge states.

- The electronic structures of carbon-incorporated gold nanowires. The results point out that two carbon atoms link neighboring gold atoms of the free-standing

nanowire, resulting in the largest breaking force and a long gold atomic spacing of 0.5 nm, in excellent agreement with the experiments. On a gold (111) surface, the gold nanowire with carbon dimer incorporation gives the gold interatomic distance of 0.5 nm, close to the value observed experimentally. The calculated formation energies indicate that the gold nanowire with carbon dimer incorporation is the most stable structure, suggesting that this one-dimensional configuration is formed on the gold surface before pulling of the STM tips.

- The electronic structures and electron-transport properties of thiol-terminated zinc porphyrin wires. I found different interface states are for the aa and hh structures, in which sulphur atoms of porphyrin molecule are bonded to gold adatoms and hollow sites of gold (111) surface. Near the Fermi level, the majorities of charge density of the aa and hh structure are confined at the molecule-electrode interfaces and at the center of porphyrin molecule, respectively. At the Fermi level, the conductance of the hh structure is one-order of magnitude smaller than that of the aa structure. In the aa structure, owing to the difference in electronegativities between sulphur and gold atoms, electrons move to the porphyrin molecule and shift the energies of the molecule states towards to the Fermi level, resulting the increased conductance.

Summary

Towards the goal of nanoscience and nanotechnology, I have investigated the electronic structures and electron-transport properties of low-dimensional systems consisting of graphene, carbon nanotube, gold nanowire, and porphyrin wire, and found that:

- By adsorption of heavy magnetic atoms or transition-metal clusters on graphene, the magnetic anisotropy energies of these systems are increased and the materials can be used as magnetized mediums in magnetic storages.

- Since carbon/boron-nitride nanotubes show spin-dependent transport behavior, they can be used as channel materials in spin field-effect transistors. Although the spin-orbit coupling in first-row elements is small, the magnetic moment of carbon/boron-nitride nanotubes can be fixed by doping heavy elements such as As or Ga, decorating the nanotubes on a magnetic surface, or bundling tubes.

- By carbon adsorption on gold (111) surface, stable one-dimensional configurations of gold nanowires with long atomic spacing due to incorporation of carbon atoms are formed on surface and these nanowires can be pulled out by scanning tunneling microscopy tip.

- By pulling and pressing molecular junction formed by thiol-terminated porphyrin wire and gold scanning tunneling microscopy tips, two conductance states can be observed, and this system can be used as active component of molecular-based switch.

Acknowledgements

The author would like to express his sincerest gratitude to Prof. Yoshitada Morikawa for continual guidance and encouragement during the course of the present work and for a critical reading of the manuscript. He is also pleased to acknowledge Prof. Tomoya Ono for fruitful discussion and encouragements. He also wishes to thank Dr. Marcus Heide and Dr. Shoichiro Saito for stimulating discussion. His thanks are also extended to all the members of the research group under Prof. Yoshitada Morikawa.

The author would like to thank the organizers Prof. Hisazumi Akai and Prof. Hideaki Kasai and participants of the QEDC Workshops and NanoScience Seminars for giving him the opportunities to get in touch with the state-of-the-art researches in this field. He is also grateful to the visitors at his poster during the GCOE symposium for constructive suggestions.

The calculation code is RSPACE developed by Prof. Tomoya Ono. This work was partially supported by the Computational Materials Science Initiative (CMSI) and by a Grant-in-Aid for Scientific Research on Innovative Areas from the Ministry of Education, Culture, Sports, Science and Technology, Japan. The numerical calculations were carried out using the computer facilities of the Institute for Solid State Physics at the University of Tokyo and Center for Computational Sciences at University of Tsukuba.

List of Publications

A. First authorship

1. N. D. Huy, N. T. Trang, L. V. Viet, N. T. Cuong and B. T. Cong, Density functional study of electronic properties of perovskite systems $La_{1-x}Sr_xFeO_3$, **J. Mater. Sci. Eng. B 2 (2012) 131**.

2. H. D. Nguyen and T. Ono, Doping effect on magnetism and transport property of heterojunction between carbon and boron nitride nanotubes, **J. Phys. Chem. C 117 (2013) 24115**.

3. H. D. Nguyen and T. Ono, Electronic structures and magnetic anisotropy energies of graphene with adsorbed transition-metal adatoms, **J. Phys. Soc. Jpn.** (accepted).

4. H. D. Nguyen and T. Ono, Electronic structures and electron-transport properties of thiol-terminated porphyrin wires (to be submitted).

B. Second authorship

1. Y. Oshima, Y. Kurui, H. D. Nguyen, T. Ono, and K. Takayanagi, Strong gold atom strands formed by incorporation of carbon atoms, **Phys. Rev. B 84 (2011) 035401.**

Conferences/Presentations

Outside Japan

1. H. D. Nguyen and T. Ono, First-Principles Study of Spin-Polarized Current in Heterostructured C/BN Nanotubes, International Conference on Nanoscience + Technology (ICN+T2012), Paris, France, July 23-27, 2012.

2. H. D. Nguyen and T. Ono, Spin Dependent Transport through Boron Carbide Nitride Nanotube, Functional Molecules on Surfaces: New Building Blocks for Nano-Spintronics CECAM/Psi-k Workshop 2012, Gustav-Stresemann-Institut, Bonn, Germany, October 2-4, 2012.

3. H. D. Nguyen and T. Ono, Magnetism and Electron Transport in C/BN Nanotube, SLAC/Stanford Summer Institute 2013: Heterogenous Catalysis for Energy Transformations, SLAC National Accelerator Laboratory, Menlo Park, USA, August 25-30, 2013.

4. H. D. Nguyen and T. Ono, Rashba Effect in Graphene with Transition-Metal Adatoms, 6^{th} Asian Workshop on First-Principles Electronic Structure Calculations, Beijing, China, October 27-30, 2013.

Inside Japan

1. H. D. Nguyen and T. Ono, First-principles Study on Spin Polarization of Zigzag Border C/BN Nanotubes, Third International Symposium on Atomically Controlled Fabrication Technology, Osaka University Nakanoshima Center, Osaka, Japan, November 24-26, 2010.

2. H. D. Nguyen and T. Ono, First-Principles Study of Transport Properties of BNC Nanotubes, 66th Annual Meeting of the Physical Society of Japan, Nigata University, Japan, March 25-28, 2011.

3. H. D. Nguyen and T. Ono, Spin-Polarized Electronic Current on C/BN Hetero-Nanotubes, Fourth International Symposium on Atomically Controlled Fabrication Technology, Osaka University Nakanoshima Center, Osaka, Japan, October 31-November 2, 2011.

4. H. D. Nguyen and T. Ono, First-principles study on spin-polarized electric current in C/BN hetero-nanotubes, The 6th Japan-Sweden Workshop on Advanced Spectroscopy of Organic Materials for Electronic Applications (ASOMEA-VI), Ishikawa, Japan, November 23-26, 2011.

5. H. D. Nguyen and T. Ono, First-principles study on transport properties of C/BN hetero-nanotubes, The 6th International Symposium on Surface Science, Tokyo, Japan, December 11-15, 2011.

6. H. D. Nguyen and T. Ono, First-Principles Study on Transport Properties of C/BN Hetero-Nanotubes, 67th Annual Meeting of the Physical Society of Japan, Kwansei Gakuin University, Kobe, Japan, March 24-27, 2012.

7. H. D. Nguyen and T. Ono, First-Principles Study on Electron-Transport Properties of CBN Hetero-Nanotubes, International Symposium on Carbon Nanotube Nanoelectronics, Nagoya, Japan, June 11-13, 2012.

8. H. D. Nguyen and T. Ono, Spin Dependent Transport in Boron Carbide Nitride Nanotube, International Symposium on Computics: Quantum Simulation and Design (ISC-QSD), Osaka, Japan, October 11-13, 2012.

9. H. D. Nguyen and T. Ono, Transport Properties of Boron Carbide Nitride Hetero-Nanotubes, Conference on Computational Physics CCP2012, Kobe, Japan, October 14-18, 2012.

10. H. D. Nguyen and T. Ono, Spin Dependent Transport in C/BN Hetero-nanotubes, Fifth International Symposium on Atomically Controlled Fabrication Technology, University Nakanoshima Center, Osaka, Japan, October 22-24, 2012.

11. H. D. Nguyen and T. Ono, Magnetism and Electron Transport in C/BN Heteronanotube, Joint Workshop of Interactive Materials Science Cadet Program (IMSC), Osaka University, and S-1 JSPS Core-to-Core Program (A) Advanced Research Networks, Awaji Yumebutai International Conference Center, Awaji-city, Japan, June 16-19, 2013.

12. H. D. Nguyen and T. Ono, Magnetism and Transport Property of Carbon/Boron Nitride Hetero-Nanotubes, Sixth International Symposium on Atomically Controlled Fabrication Technology, Osaka University Nakanoshima Center, Osaka, Japan, February 5-6, 2014.

13. H. D. Nguyen and T. Ono, Rashba Spin-Orbit Coupling in Graphene Doped with Transition Metals, 6th International Symposium on Advanced Plasma Science and its Applications for Nitrides and Nanomaterials/ 7th International Conference on Plasma-Nano Technology & Science, Meijo University, Nagoya, Japan, March 2-6, 2014.

14. H. D. Nguyen and T. Ono, Rashba Effect in Graphene Doped with Transition Metals, 69th Annual Meeting of the Physical Society of Japan, Shonan campus, Tokai University, Kanagawa, Japan, March 27-30, 2014.

Bibliography

[1] T. Ono, T. Ota, and Y. Egami. *Phys. Rev. B*, 84:224424, 2011.

[2] L. Ci, L. Song, C. Jin, D. Jariwala, DangxinWu, Y. Li, A. Srivastava, Z. F. Wang, K. Storr, L. Balicas, F. Liu, and P. M. Ajayan. *Nat. Mat.*, 9:430, 2010.

[3] S. Enouz, O. Stephan, J.-L. Cochon, C. Colliex, and A. Loiseau. *Nano Lett.*, 7: 1856, 2007.

[4] T. Ono, Y. Egami, and K. Hirose. *Phys. Rev. B*, 86:195406, 2012.

[5] Y. Oshima, Y. Kurui, H. D. Nguyen, T. Ono, and K. Takayanagi. *Phys. Rev. B*, 84:035401, 2011.

[6] Z. Li, T.-H. Park, J. Rawson, M. J. Therien, and E. Borguet. *Nano Lett.*, 12:2722, 2012.

[7] P. Hohenberg and W. Kohn. *Phys. Rev.*, 136:B864, 1964.

[8] W. Kohn and L. J. Sham. *Phys. Rev.*, 140:A1133, 1965.

[9] R. M. Martin. *Electronic Structure Basic Theory and Practical Methods*. Cambridge University Press, The Edinburgh Building, Cambridge CB2 2RU, UK, 2004.

[10] G. B. Bachelet, D. R. Hamann, and M. Schluter. *Phys. Rev. B*, 26:4199, 1982.

[11] D. R. Hamann, M. Schluter, and C. Chiang. *Phys. Rev. Lett.*, 43:1494, 1979.

[12] N. Troullier and J. L. Martins. *Phys. Rev. B*, 43:1993, 1991.

[13] D. Vanderbilt. *Phys. Rev. B*, 41:7892, 1985.

[14] K. Laasonen, R. Car, C. Lee, and D. Vanderbilt. *Phys. Rev. B*, 43:6796, 1991.

[15] J. R. Chelikowsky, N. Troullier, and Y. Saad. *Phys. Rev. Lett.*, 72:1240, 1994.

[16] K. Hirose, T. Ono, Y. Fujimoto, and S. Tsukamoto. *First-Principles Calculations in Real-Space Formalism, Electronic Configurations and Transport Properties of Nanostructures*. Imperial College Press, 57 Shelton Street, Covent Garden, London WC2H 9HE, 2005.

[17] R. Landauer. *Philosophical Magazine*, 21:863, 1970.

[18] D. D. Koelling and B. N. Harmon. *J. Phys. C: Solid St. Phys.*, 10:3107, 1977.

[19] A. H. MacDonald, W. E. Pickett, and D. D. Koelling. *J. Phys. C: Solid St. Phys.*, 13:2675, 1980.

[20] C. Li, A. J. Freeman, H. J. F. Jansen, and C. L. Fu. *Phys. Rev. B*, 42:5433, 1990.

[21] L. Szunyogh, B. Újfalussy, and P. Weinberger. *Phys. Rev. B*, 51:9552, 1995.

[22] H. J. Jansen. *Phys. Rev. B*, 59:4699, 1999.

[23] M. Gyamfi, T. Eelbo, S. Forti U. Starke A. I. Lichtenstein M. I. Katsnelson M. Wásniowska, T. O. Wehling, and R. Wiesendanger. *Phys. Rev. B*, 85: 161406(R), 2012.

[24] Z. Qiao, S. A. Yang, W. Feng, W.-K. Tse, J. Ding, Y. Yao, J. Wang, and Qian Niu. *Phys. Rev. B*, 82:161414(R), 2010.

[25] T. Eelbo, M. Waśniowska, P. Thakur, M. Gyamfi, B. Sachs, T. O. Wehling, S. Forti, U. Starke, C. Tieg, A. I. Lichtenstein, and R. Wiesendanger. *Phys. Rev. Lett.*, 110:136804, 2013.

[26] M. Sargolzaei and F. Gudarzi. *J. Appl. Phys.*, 110:064303, 2011.

[27] C. D. Porter and D. Stroud. *Phys. Rev. B*, 85:235452, 2012.

[28] T. Ono and K. Hirose. *Phys. Rev. Lett.*, 82:5016, 1999.

[29] T. Ono and K. Hirose. *Phys. Rev. B*, 72:085115, 2005.

[30] T. Ono, M. Heide, N. Atodiresei, P. Baumeister, S. Tsukamoto, and S. Blügel. *Phys. Rev. B*, 82:205115, 2010.

[31] P. E. Blöchl. *Phys. Rev. B*, 50:17953, 1994.

[32] S. H. Vosko, L. Wilk, and M. Nusair. *Can. J. Phys.*, 58:1200, 1980.

[33] T. Eelbo, M. Wásniowska, M. Gyamfi, S. Forti, U. Starke, and R. Wiesendanger. *Phys. Rev. B*, 87:205443, 2013.

[34] J. Ding, Z. Qiao, W. Feng, Y. Yao, and Q. Niu. *Phys. Rev. B*, 84:195444, 2011.

[35] T. O. Wehling, A. I. Lichtenstein, and M. I. Katsnelson. *Phys. Rev. B*, 84:235110, 2011.

[36] T. O. Wehling, A. V. Balatsky, M. I. Katsnelson, A. I. Lichtenstein, and A. Rosch. *Phys. Rev. B*, 81:115427, 2010.

[37] H. Johll, H. C. Kang, and E. S. Tok. *Phys. Rev. B*, 79:245416, 2009.

[38] C. Cao, M. Wu, J. Jiang, and H.-P. Cheng. *Phys. Rev. B*, 81:205424, 2010.

[39] A. Y. Liu, R. M. Wentzcovitch, and M. L. Cohen. *Phys. Rev. B*, 39:1760, 1989.

[40] Y. Virgus, W. Purwanto, H. Krakauer, and S. Zhang. *Phys. Rev. B*, 86:241406(R), 2012.

[41] A. N. Rudenko, F. J. Keil, M. I. Katsnelson, and A. I. Lichtenstein. *Phys. Rev. B*, 86:075422, 2012.

[42] K. T. Chan, J. B. Neaton, and M. L. Cohen. *Phys. Rev. B*, 77:235430, 2008.

[43] M. Gmitra, S. Konschuh, C. Ertler, C. Ambrosch-Draxl, and J. Fabian. *Phys. Rev. B*, 80:235431, 2009.

[44] C. F. Hirjibehedin, C. Lin, A. F. Otte, M. Ternes, C. P. Lutz, B. A. Jones, and A. J. Heinrich. *Science*, 317:1199, 2007.

[45] F. Varchon, R. Feng, J. Hass, X. Li, B. N. Nguyen, C. Naud, P. Mallet, J.-Y. Veuillen, C. Berger, E. H. Conrad, and L. Magaud. *Phys. Rev. Lett.*, 99:126805, 2007.

[46] M. Fujita, K. Wakabayashi, K. Nakada, and K. Kusakabe. *J. Phys. Soc. Jpn.*, 65: 1920, 1996.

[47] M. Kohmoto and Y. Hasegawa. *Phys. Rev. B*, 76:205402, 2007.

[48] S. Okada and A. Oshiyama. *Phys. Rev. Lett.*, 87:146803, 2001.

[49] E. H. Lieb. *Phys. Rev. Lett.*, 62:1201, 1989.

[50] K. Yuge. *Phys. Rev. B*, 79:144109, 2009.

[51] O. Hod and G. E. Scuseria. *ACS Nano*, 2:2243, 2008.

[52] S. Okada and A. Oshiyama. *J. Phys. Soc. Jpn.*, 72:1510, 2003.

[53] J. Choi, Y.-H. Kim, K. J. Chang, and D. Tomanek. *Phys. Rev. B*, 6:125421, 2003.

[54] L. Chico and W. Jaskóski. *Phys. Rev. B*, 69:085406, 2004.

[55] K. Kobayashi. *Comput. Mater. Sci.*, 14:72, 1999.

[56] J. P. Perdew and A. Zunger. *Phys. Rev. B*, 31:6207, 1981.

[57] Y. Fujimoto and K. Hirose. *Phys. Rev. B*, 67:195315, 2003.

[58] L. Kong, J. R. Chelikowsky, J. B. Neaton, and S. G. Louie. *Phys. Rev. B*, 76: 235422, 2007.

[59] M. Buttiker, Y. Imry, R. Landauer, and S. Pinhas. *Phys. Rev. B*, 31:6207, 1985.

[60] M. Ouyang, J.-L. Huang, C. L. Cheung, and C. M. Lieber. *Science*, 292:702, 2001.

[61] T. Miyake and S. Saito. *Phys. Rev. B*, 72:073404, 2005.

[62] X. Blase, A. Rubio, S. G. Louie, and M. L. Cohen. *Europhys. Lett.*, 28:335, 1994.

[63] W. Wang, Y. Xia, N. Xu, and Z. Li. *J. Phys. Chem. C*, 113:17313, 2009.

[64] J. Janak. *Phys. Rev. B*, 16:255, 1977.

[65] M. M. Sigalas and D. A. Papaconstantopoulos. *Phys. Rev. B*, 50:7255, 1994.

[66] J. I. Pascual, J. M'eendez, J. Góomez-Herrero, A. M. Baróo, N. García, , and V. T. Binh. *Phys. Rev. Lett.*, 71:1852, 1993.

[67] L. Olesen, E. Laegsgaard, I. Stensgaard, F. Besenbacher, J. Schiotz, P. Stoltze, K. W. Jacobsen, and J. K. Norskov. *Phys. Rev. Lett.*, 72:2251, 1994.

[68] M. Brandbyge, J. Schiotz, M. R. Sorensen, P. Stoltze, K. W. Jacobsen, J. K. Norskov, L. Olesen, E. Laegsgaard, I. Stensgaard, and F. Besenbacher. *Phys. Rev. B*, 52:8499, 1995.

[69] H. Ohnishi, Y. Kondo, and K. Takayanagi. *Nature*, 395:780, 1998.

[70] A. I. Yanson, G. R. Bollinger, H. E. van Den Brom, N. Agrait, and J. M. van Ruitenbeek. *Nature*, 395:783, 1998.

[71] J. M. Krans, C. J. Muller, I. K. Yanson, Th. C. M. Govaert, R. Hesper, and J. M. van Ruitenbeek. *Phys. Rev. B*, 48:14721, 1993.

[72] J. M. Krans, J. M. van Ruitenbeek, V. V. Fisun, I. K. Yanson, and L. J. De Jongh. *Nature*, 375:767, 1995.

[73] G. Rubio, N. Agraıt, and S. Vieira. *Phys. Rev. Lett.*, 76:2302, 1996.

[74] G. R. Bollinger, S. R. Bahn, N. Agraıt, K. W. Jacobsen, and S. Vieira. *Phys. Rev. Lett.*, 87:026101, 2001.

[75] U. Landman, W. D. Luedtke, N. A. Burnham, and R. J. Colton. *Science*, 248:454, 1990.

[76] F. D. Novaes, A. J. R. da Silva, E. Z. da Silva, and A. Fazzio. *Phys. Rev. Lett.*, 96:016104, 2006.

[77] W. H. A. Thijssen, D. Marjenburgh, R. H. Bremmer, and J. M. van Ruitenbeek. *Phys. Rev. Lett.*, 96:026806, 2006.

[78] F. D. Novaes, A. J. R. da Silva, E. Z. da Silva, and A. Fazzio. *Phys. Rev. Lett.*, 90:036101, 2003.

[79] Sz. Csonka, A. Halbritter, and G. Mihály. *Phys. Rev. B*, 73:075405, 2006.

[80] E. Anglada, J. A. Torres, F. Yndurain, and J. M. Soler. *Phys. Rev. Lett.*, 98: 096102, 2007.

[81] Y. Zhang, Y.-W. Tan, H. L. Stormer, and P. Kim. *Nature (London)*, 438:201, 2005.

[82] E. Hobi Jr., A. Fazzio, and A. J. R. da Silva. *Phys. Rev. Lett.*, 100:056104, 2008.

[83] T. Kizuka. *Phys. Rev. B*, 77:155401, 2008.

[84] Y. Oshima, K. Mouri, H. Hirayama, and K. Takayanagi. *Surf. Sci.*, 531:209, 2003.

[85] S. B. Legoas, D. S. Galvao, V. Rodrigues, and D. Ugarte. *Phys. Rev. Lett.*, 88: 076105, 2002.

[86] S. B. Legoas, D. S. Galvao, V. Rodrigues, and D. Ugarte. *Phys. Rev. Lett.*, 88: 076105, 2002.

[87] S. Tsukamoto, T. Ono, Y. Fujimoto, K. Inagaki, H. Goto, and K. Hirose. *Materials Transactions*, 42:2257, 2001.

[88] A. Nitzan and M. A. Ratner. *Science*, 300:1384, 2003.

[89] B. Q. Xu and N. J. Tao. *Science*, 301:1221, 2003.

[90] R. L. McCreery and A. J. Bergren. *Adv. Mater.*, 21:4303, 2009.

[91] S. J. Molen and P. Liljeroth. *J. Phys.: Condens. Matter*, 22:133001, 2010.

[92] L. Scullion, T. Doneux, L. Bouffier, D. G. Fernig, S. J. Higgins, D. Bethell, and R. J. Nichols. *J. Phys. Chem. C*, 115:8361, 2011.

[93] G. Sedghi, K. Sawada, L. J. Esdaile, M. Hoffmann, H. L. Anderson, D. Bethell, W. Haiss, S. J. Higgins, and R. J. Nichols. *J. Am. Chem. Soc.*, 130:8582, 2008.

[94] L. Venkataraman, J. E. Klare, C. Nuckolls, M. S. Hybertsen, and M. L. Steigerwald. *Nature*, 442:904, 2006.

[95] Y. J. Xing, T.-H. Park, R. Venkatramani, S. Keinan, D. N. Beratan, M. J. Therien, and E. Borguet. *J. Am. Chem. Soc.*, 132:7946, 2010.

[96] D. T. Gryko, C. Clausen, K. M. Roth, N. Dontha, D. F. Bocian, W. G. Kuhr, and J. S. Lindsey. *J. Org. Chem.*, 65:7345, 2000.

[97] K. M. Roth, D. T. Gryko, C. Clausen, J. Li, J. S. Lindsey, W. G. Kuhr, and D. F. Bocian. *J. Phys. Chem. B*, 106:8639, 2002.

[98] H. Hoppe and N. S. Sariciftci. *J. Mater. Res.*, 19:1924, 2004.

[99] D. Kruger, H. Fuchs, R. Rousseau, D. Marx, and M. Parrinello. *Phys. Rev. Lett.*, 89:186402, 2002.

[100] M. Di Ventra, S. T. Pantelides, and N. D. Lang. *Phys. Rev. Lett.*, 84:979, 2000.

[101] N. Sergueev, L. Tsetseris, K. Varga, and S. Pantelides. *Phys. Rev. B*, 82:073106, 2010.

[102] X. Li, J. He, J. Hihath, B. Xu, S. M. Lindsay, and N. Tao. *J. Am. Chem. Soc.*, 128:2135, 2006.

[103] S. Y. Quek, M. Kamenetska, M. L. Steigerwald, H. J. Choi, S. G. Louie, M. S. Hybertsen, J. B. Neaton, and L. Venkataraman. *Nature Nanotech.*, 4:230, 2009.

[104] M. Strange, C. Rostgaard, H. Hakkinen, and K. S. Thygesen. *Phys. Rev. B*, 83: 115108, 2011.

[105] R. J. C. Batista, P. Ordejon, H. Chacham, and E. Artacho. *Phys. Rev. B*, 75: 041402(R), 2007.

[106] C. B. Madsen, L. B. Madsen, S. S. Viftrup, M. P. Johansson, T. B. Poulsen, L. Holmegaard, V. Kumarappan, K. A. Jørgensen, and H. Stapelfeldt. *Phys. Rev. Lett.*, 102:073007, 2009.

[107] C. B. Madsen, L. B. Madsen, S. S. Viftrup, M. P. Johansson, T. B. Poulsen, L. Holmegaard, V. Kumarappan, K. A. Jørgensen, and H. Stapelfeldt. *J. Chem. Phys.*, 130:234310, 2009.

[108] S. Ramakrishna and T. Seideman. *Phys. Rev. Lett.*, 99:103001, 2007.

[109] E. G. Emberly and G. Kirczenow. *Phys. Rev. B*, 58:10911, 1998.

[110] P. E. Kornilovitch and A. M. Bratkovsky. *Phys. Rev. B*, 64:195413, 2001.

[111] J. T. Obodo, K. Gkionis, I. Rungger, S. Sanvito, and U. Schwingenschlogl. *Phys. Rev. B*, 88:085438, 2013.

[112] Z. Ning, J. Chen, S. Hou, J. Zhang, Z. Liang, J. Zhang, and R. Han. *Phys. Rev. B*, 72:155403, 2005.